Wettability Evolution of Sandpacks with Clay Content during Long-Term Waterflooding: A Pore-Scale Contact Angle Characterization

Chaodong Xi[1], Wenbo Gong[2], Xukang Lu[1], Guang Yang[1], Yang Ju[3], and Moran Wang[1]*

[1]Department of Engineering Mechanics, Tsinghua University, Beijing
[2]College of Safety and Ocean Engineering, China University of Petroleum, Beijing
[3]State Key Laboratory for Fine Exploration and Intelligent Development of Coal Resources, China University of Mining and Technology, Beijing

Summary

Wettability of rocks may undergo a dynamic evolution during long-term waterflooding. Existing studies usually assume a constant wettability property of rock and ignore the wettability evolution during long-term waterflooding, resulting in ambiguous recognition of residual oil resources. To uncover the wettability evolution within complex pore structure, the effects of clay content on local contact angles are addressed in the sandpacks during long-term waterflooding via in-situ computed tomography (CT) imaging experiments. In this study, the wettability evolution is quantitatively characterized by mean contact angle, contact angle hysteresis, and wettability representative element volume (REV) size. Based on surface roughness and clay deposition patterns, we propose a physical model to analyze the mechanism of wettability evolution. The results indicate that the contact angle distribution within the pore structure is heterogeneous while locally continuous. Water-clay turbid treatment is effective in altering the wetting state of sandpack to less water-wet, reducing the contact angle hysteresis, and enhancing the heterogeneity of contact angle distribution. Waterflooding makes the sandpacks more water-wet and decreases the heterogeneity of contact angle distribution. Transition of surface roughness and clay deposition patterns during waterflooding accounts for the contact angle alteration and determines the overall wettability evolution.

Introduction

During oilfield development, the waterflooding process may take decades to recover the subsurface oil. However, the recovery rates in oil fields fall short of expectations; even after long-term waterflooding, it is often observed that about 25–50% of the oil remains within the reservoir (Bai et al. 2022). Long-term waterflooding leads to a complicated wettability evolution of reservoir rock, the characteristics and mechanisms of which remain unclear (Liu and Wang 2020).

Natural rocks exhibit significant heterogeneity in chemical composition, grain surface roughness, and clay content, resulting in the heterogeneity of their wettability (Shi et al. 2023; Caruana and Dawe 1996; Arshadi et al. 2020). Thus, it is often difficult to obtain consistent results through traditional macroscopic plate contact angle tests to characterize rock wettability (Drelich 2019). A more commonly used method is to reflect the wettability of rocks through the wettability index at the core scale, including the Amott index (Amott 1959) and the U.S. Bureau of Mines index (Donaldson et al. 1969). However, there exists uncertainty when attempting to quantitatively assess the wettability of rocks using the two wettability indices (Anderson 1986). The basis of the Amott index and U.S. Bureau of Mines index are the volume of fluid spontaneous imbibition and macroscopic capillary force in the experiment, which are not solely determined by wettability. For example, for two pore systems with identical wettability, changing the pore structure likely induces changes in the spontaneous imbibition volume and capillary force and results in variation of the experimentally measured wettability index. Considering the common differences in the pore structure of natural rocks (Reynolds et al. 2018; Ott et al. 2014; Arzilli et al. 2016), the wettability index should not be used as a rigorous quantitative description method for rock wettability but can only serve as a qualitative reference. More importantly, these two wettability indices represent the average wettability of all pore walls in rocks, ignoring the local and nonuniform distribution of wettability in the 3D pores of rocks (Armstrong et al. 2021). The local displacement events that affect the overall multiphase flow behavior are directly controlled by the local wetting characteristics of the pore wall (Geistlinger and Ataei-Dadavi 2015; Lei et al. 2023; Shokri and Or 2013). The limitations of traditional description in characterizing rock wettability, coupled with the incomplete understanding of local wettability characteristics within rock pores, pose a formidable challenge in the intricate wettability mechanisms within the 3D pore structure of rocks. With the advancement of CT imaging and image analysis technology, the characterization of rock wettability has made some new progress in the past decade (Wildenschild and Sheppard 2013; Cnudde and Boone 2013; Saif et al. 2019). In 2014 (Andrew et al. 2014), an in-situ measurement method for local contact angles at the pore scale was proposed and applied to characterize the wettability of CO_2-water-rock three-phase systems. This method features the local measurement of contact angle at the three-phase contact line within the pore structure and uses sufficient measurement results of contact angle to form a probability density distribution. More studies (Klise et al. 2016; AlRatrout et al. 2017; Yang and Zhou 2020) further improved the measurement method of contact angle by using different curve fitting strategies and automated measurement algorithms to achieve accurate and efficient measurement of local contact angle. Compared to the traditional wettability index, the pore-scale contact angle measurement provides much more information about the rock wetting state. It is based on local measurement of contact angle within pore structures and uses a contact angle

*Corresponding author; email: mrwang@tsinghua.edu.cn

Copyright © 2025 Society of Petroleum Engineers

Original SPE manuscript received for review 22 May 2024. Revised manuscript received for review 13 October 2024. Paper (SPE 223938) peer approved 28 October 2024. Supplementary materials are available in support of this paper and have been published online under Supplementary Data at https://doi.org/10.2118/223938-PA. SPE is not responsible for the content or functionality of supplementary materials supplied by the authors.

Downloaded from http://onepetro.org/SJ/article-pdf/30/01/180/4110338/spe-223938-pa.pdf/1 by Tsinghua University user on 15 May 2025

distribution function instead of a single wettability index to quantitatively characterize the wettability of rocks. This method shows a clearer and more accurate physical meaning and can reflect the nonuniform characteristics of the wettability of natural rock.

Wettability manipulates the multiphase displacement behavior via pore-scale displacement events such as snap-off, cooperative pore filling, film flow, and Haines' jump (Singh et al. 2017, 2022; Holtzman and Segre 2015; Moura et al. 2019; Berg et al. 2013). The current work mainly focuses on the influence and mechanism of different wettability states on water-oil displacement behavior and displacement efficiency (Herring et al. 2016; Liu et al. 2023). A previous study indicates that the competition of pore-scale displacement events results in a nonmonotonic effect of wettability on water-oil displacement efficiency (Lei et al. 2022). It is believed that the weak water-wet, neutral-wet, or mixed wettability are favorable for the enhancement of water-oil displacement efficiency (Alnoush et al. 2022). Many water-based enhanced oil recovery technologies have been applied to the oil field, including low-salinity flooding (Belhaj et al. 2023a, 2023b), alkaline/surfactant/polymer flooding (Laben et al. 2022), smart waterflooding (Belhaj et al. 2024), and nanoparticle-enhanced flooding (Fakir et al. 2023). Wettability evolution plays an important role for the success of these enhanced oil recovery technologies (Belhaj et al. 2022; Sarma et al. 2022). In experiments, different micromodel materials or rock aging techniques are used to regulate wettability (Buckley et al. 1998; Mohammed and Babadagli 2015). However, these works did not consider the dynamic changes in wettability during the water-oil displacement process and are referred to as static wettability studies. It has been observed that oil production can still be obtained, even after decades of waterflooding, but in laboratory waterflooding experiments using micromodels or rock cores, oil flow may usually stop immediately after the breakthrough of water (Ju et al. 2019). The wettability evolution of reservoir rock over a long-term waterflooding process accounts for the observed difference. The chemical or physical properties of the micromodel materials are relatively stable, and their wettability is believed to be constant during water-oil displacement (Gerami et al. 2018). Before the rock waterflooding test, core cleaning is a standard procedure during which a large volume of organic solvent is forced to flow through the rock core to remove the initial oil within the pore structure (Herring et al. 2018). At the same time, some materials within pore structure that may lead to wettability alteration during waterflooding are also flashed away during the core cleaning process. Therefore, the wettability of rock cores during waterflooding is treated as a constant state in most laboratory experiments. However, for subsurface reservoir rocks, long-term waterflooding may flash away clay minerals on the pore surface and corrode the pore walls, leading to a continuous wettability evolution of reservoir rocks. The wettability evolution disturbs the flow field in the reservoir and leads to the continuous evolution of the occurrence and distribution of residual oil. Due to the wide impact area and long production cycle of waterflooding development in the reservoir, ignoring the dynamic wettability evolution of reservoir rock will inevitably lead to an erroneous estimation of the effectiveness of waterflooding development (Khishvand et al. 2019). At present, there is relatively little research on the dynamic evolution of rock wettability. Existing work indicates that possible factors affecting the dynamic changes of rock wettability include heterogeneity of fluid flow in formation rock pores (Lei et al. 2022), adsorption and desorption of polar compounds and asphaltene in crude oil on solid walls (Buckley et al. 1997; Mamonov et al. 2019; Zhang et al. 2022; Cao et al. 2015), changes in formation water salinity and pH (Khishvand et al. 2017; Selem et al. 2021), dissolution of minerals on rock pore walls (Menke et al. 2014), instability of oil films on rock pore walls (Singh et al. 2016), and clay content in rock (Borysenko et al. 2009; Li et al. 2023; Wang et al. 2022). The mechanism of these factors is complex and unclear, and they also affect and interact with each other. Our understanding of wettability and its underlying evolution law remains incomplete. It is extremely challenging to establish a quantitative model to describe the dynamic evolution law of rock wettability based on these factors. In numerical simulation, the contact angle is generally directly used as a parameter input for flow calculation in the model (Cha et al. 2023). Due to the lack of an accurate description of the dynamic evolution law of wettability, most existing simulation analyses associated with dynamic wettability are still in the preliminary exploration stage (Liu and Wang 2022). Therefore, it is vital to address the dynamic evolution law of rock wettability during long-term waterflooding.

To uncover the rock wettability evolution during long-term waterflooding, we chose clay content as the main factor and characterized its impacts on rock wettability evolution. We applied in-situ CT imaging and angle measurement at a three-phase contact line to obtain contact angle distribution in 3D pore structure during long-term waterflooding, which addressed the limitations of the traditional wettability index. Because a three-phase contact line may not be sufficient or homogeneously distributed in the pore space, we applied a water-oil coinjection procedure after each waterflooding stage to create a sufficient three-phase contact line and ensure the representativeness of contact angle measurement. We characterized quantitatively the impacts of clay content and waterflooding on sandpack wettability by mean contact angle, contact angle hysteresis, and wettability REV size. We present and discuss the direct 3D visualization of contact angle distribution and its evolution within pore space, the variation of mean contact angle, the contact angle hysteresis, and the wettability REV size during waterflooding. In addition, we propose a physical model considering surface roughness and clay deposition patterns to analyze the mechanism of wettability evolution. The findings and results of this study provide valuable insights for rock wettability evolution subjected to long-term waterflooding, which is crucial for further wettability model establishment and residual oil recovery enhancement.

Materials and Methods

Materials. Nature rocks are extremely complex and characterized by complex pore geometries, mixed mineral compositions, and heterogeneous permeability. These factors have impacts on the wettability evolution behavior during waterflooding. The current work is a fundamental study that focuses on the impacts and mechanisms of clay content on the wettability evolution behavior during waterflooding. To achieve this goal, we should eliminate the impacts of other factors. We used clean quartz sand instead of nature rocks as the testing porous media to ensure a consistent initial state across the tests, including pore geometry, grain surface property, and permeability. The average diameter of the selected quartz sand is 0.8 mm. The sand grain features an irregular shape and a rough surface. Microscopic images of the quartz sand used in the experiment are provided in **Fig. S-1** in the Supplementary Material. The quartz sand was packed in a plastic column with a diameter of 15 mm. After compaction, the porosity of the sandpack in the column is about 41%, estimated from the 3D CT image. Key parameters are summarized in **Table 1**. Kaolinite was chosen as the testing clay because it is a commonly observed clay mineral in the reservoir and may play a crucial role in wettability alteration. In addition, kaolinite can be easily dispersed in water and forms a relatively stable clay-water turbid but it can hardly be dispersed in oil. In this study, we added clay to the sandpack by clay-water turbid flooding. Thus, the initial clay content in the sandpack can be manipulated by adjusting the clay content of the clay-water turbid.

Brine and oil were prepared for the long-term waterflooding test. Water doped with 5 wt% NaI was used as the brine phase due to its good performance as CT contrast agent (Lusic and Grinstaff 2013). A mixture of 40 wt% crude oil and 60 wt% mineral oil was prepared as the oil phase. Liquid parameters are listed in **Table 2**. This study aims to investigate the effects of clay minerals on the wettability of sandpacks during long-term waterflooding via in-situ CT imaging and pore-scale contact angle measurement techniques. The experimental objects and methods require clear and accurate segmentation of grain, oil, and water phases from the CT image. Although the brine composition is not representative of actual injected brine, the currently used brine provides the necessary foundation for CT imaging and the following image analysis.

Downloaded from http://onepetro.org/SJ/article-pdf/30/01/180/4110338/spe-223938-pa.pdf/1 by Tsinghua University user on 15 May 2025

Parameter	Value
Porosity	41%
Pore volume	6.3 cm^3
Permeability	164.3 darcies
Grain size	0.8 mm
Diameter of sandpack	15 mm

Table 1—Key parameters of the sandpack.

Parameter	Brine Phase	Oil Phase
Density	1.03 g/cm^3	0.80 g/cm^3
Viscosity	1.48 mPa·s	34.32 mPa·s
Interfacial tension	19.64 mN/m	

Table 2—Liquid parameters of the brine phase and oil phase.

Experimental Apparatus and Procedure. The experimental system includes a microfocus X-ray generator, a rotation device, an image acquisition device, a fluid displacement testing device, and a control device, as shown in **Fig. 1a**. The voxel resolution of the 3D CT images is up to 15 μm, which allows us to observe and identify the solid, brine, and oil phases accurately. In this study, the voltage and current of the microfocus X-ray generator were set as 120 kV and 0.2 mA, respectively. It took approximately 40 minutes to finish one CT scanning process and acquire 1,440 projection images at 2048×2048 plane resolution.

To characterize the wettability evolution of sandpacks during long-term waterflooding, we designed an experimental protocol and focused on contact angle measurement at pore scale. The procedures are demonstrated in **Fig. 1b**. First, the prepared sandpack column was flooded with water-clay turbid to add the clay content to the sandpack. We designed two testing groups and one control group. For the testing groups, the sandpacks were flooded by 10 wt% water-clay turbid and 20 wt% water-clay turbid, respectively. For the control group, the sandpack was flooded by deionized water. The injection rate of water-clay turbid or deionized water was 1 mL/min, and the flooding process lasted for 1 hour. To ensure that the clay was deposited on the grain surface, the sandpack columns were placed on a bedstand and kept from disturbance for 12 hours after flooding, and then the oil phase was injected into the sandpack columns at 1 mL/min for 1 hour to displace the liquid in the pore space. We waited for another 12 hours until the mechanical and chemical balance state was established in the sand-brine-oil-clay system. For conciseness, the clean sandpack, the sandpack treated with 10 wt% water-clay turbid, and the sandpacks treated with 20 wt% water-clay turbid are referred to as Sandpack A, Sandpack B, and Sandpack C, respectively. We designed three groups of tests with various initial clay content, and the uncertainty in replicating the wettability condition should be considered. In this study, we paid more attention to the wettability evolution trend in each experiment instead of the comparison across different experiments.

We carried out three groups of the in-situ waterflooding experiments with the same experimental procedures: (1) Waterflooding—the brine was injected into the sandpack at a rate of 1 mL/min for different pore volumes (PV) of 1 PV, 5 PV, 10 PV, or 50 PV according to the experiment stage. For the sandpack prepared in the experiment, 1 PV equals 6.3 mL. The capillary number is defined as $Ca = \mu_b u_b/\sigma_{ob}$, where μ_b is the viscosity of the brine, u_b is the displacement velocity, and σ_{ob} refers to the interfacial tension between oil and brine phase. Based on the parameters listed in **Table 1**, the capillary number of the displacement process was 1.74×10^{-5}. (2) Water-oil coinjection: Because we assess the wettability of the sandpack by the local contact angle at pore scale, adequate measurement of the local contact angle is the prerequisite for the precise characterization of the wetting state. However, owing to the preferential flow during long-term waterflooding, the residual oil and three-phase contact lines may not be sufficient for wettability estimation. Thus, the measurement result may lose its generality if the local contact angle at pore scale is measured after the waterflooding step immediately. To address this issue, brine and oil were injected into the sandpack simultaneously after waterflooding to create sufficient and diverse water-oil interfaces or three-phase contact lines. Two syringe pumps were used in this step, and the rate for brine and oil was 0.75 mL/min and 0.25 mL/min, respectively. The total volume of water-oil injection was 1 PV. (3) CT scanning: The configuration of the water and oil phases in the pore space was captured and recorded via CT scanning. Then, the contact angles at pore scale were measured from the 3D CT images by a self-developed computation algorithm. Steps 1 through 3 were repeated in the successive waterflooding stage, except that the water injection volume in Step 1 was different. A detailed explanation about the capillary number, the injection rate, and the impacts of water-oil coinjection is provided in the Supplementary Material.

CT Image Processing and Contact Angle Measurement. The CT images of the experiment were filtered and segmented using the software Avizo®. All the CT image data sets were processed following the procedures shown in **Figs. 2a through 2c**. In the original CT image **(Fig. 2a)**, the light gray, dark gray, and black parts indicate the solid, water, and oil phases, respectively. To suppress the image noise, a 3D nonlocal mean filter (Buades et al. 2008) was applied, as shown in **Fig. 2b**. A watershed-based segmentation method (Schlüter et al. 2014) was applied to segment the image into a solid phase, oil phase, and water phase, as depicted in **Fig. 2c**. The yellow, gray, and cyan colors indicate the oil, solid, and water phases, respectively, and the corresponding 3D visualization of the grain, water, and oil phases is shown in **Figs. 2d and 2e**. All the following visualization and quantitative measurements were based on the 3D digital rocks with segmented phases.

Downloaded from http://onepetro.org/SJ/article-pdf/30/01/180/4110338/spe-223938-pa.pdf/1 by Tsinghua University user on 15 May 2025

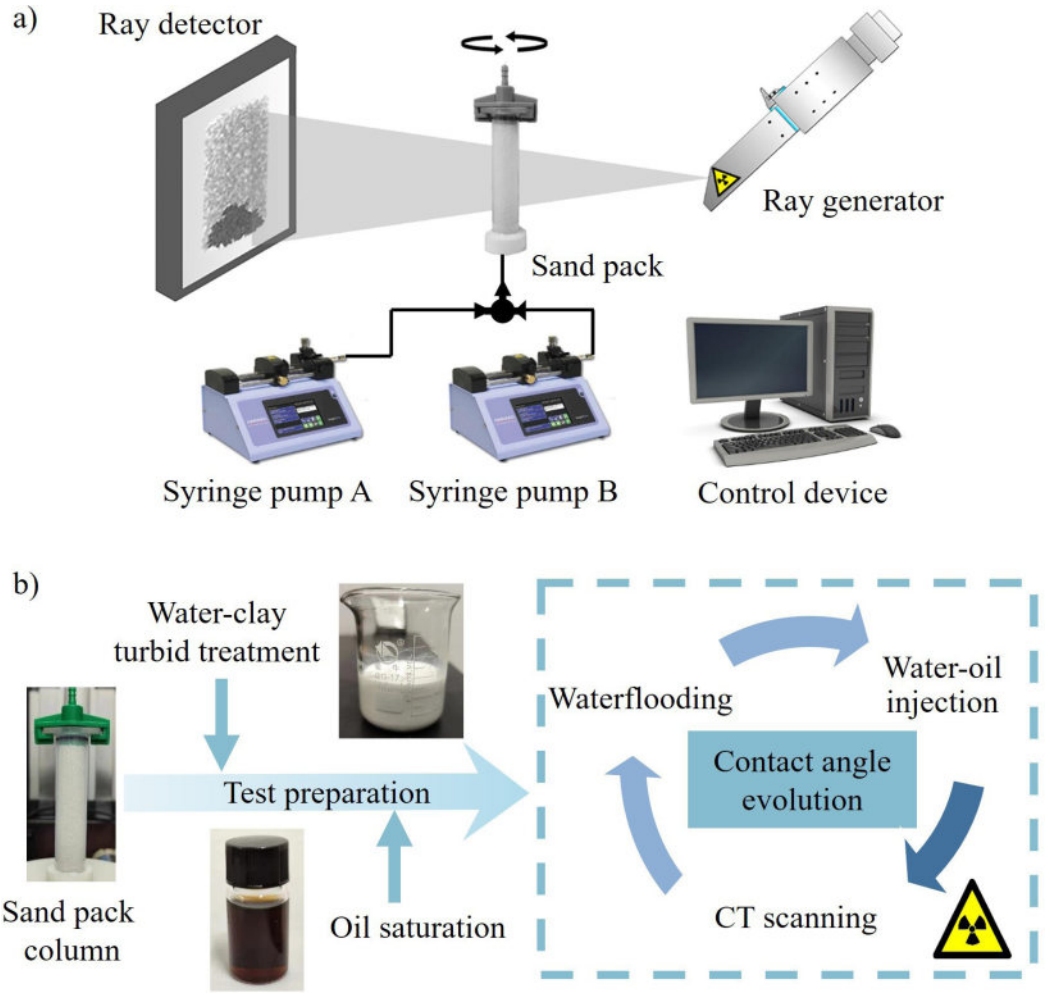

Fig. 1—Experimental setup, materials, and strategy: (a) schematic representation of the experimental equipment and (b) schematic map of the experimental procedures.

The measurement of contact angle at pore scale requires one to determine the angle along the three-phase contact line by (1) identifying the three-phase boundary (three-phase contact line) of the system based on the segmented rock, oil, and water phases; (2) determining the normal plane at one measurement point on the three-phase contact line; (3) specifying the tangent lines of the oil-water interface and the water-rock interface at the measurement point within that plane; and (4) calculating the local contact angle at that point that equals to the angle between the two tangent lines. Based on a large amount of measurement data, the probability density distribution of contact angles is obtained to quantitatively characterize the wettability of rocks. A detailed description of the algorithm can be found in a previous study (Andrew et al. 2014; Lv et al. 2017). Discussion about the precision and repeatability of the used methods is provided in **Figs. S-3 and S-4** of the Supplementary Material.

Results and Discussion

Wettability Alteration by Water-Clay Turbid Treatment. To better demonstrate the effect of water-clay turbid treatment on the sandpack's wettability, the measurement results of contact angle were visualized within the pore structures, as shown in **Figs. 3a through 3c**. In the images, cubic boxes indicate the cropped volume from the processed CT image data set, so that the values of the local contact angle can be exhibited directly. The side length of the boxes is 250 voxels (3.75 mm). The dark parts in the image are the sand grains. The curves on the grain surface indicate the three-phase contact lines and the colors correspond to the value of the local contact angle. Because there is only a small amount of three-phase contact points whose angles are smaller than 40° or larger than 90° in the results, these data points are rendered in blue or red to maintain sharp color contrast. In the images, it can be observed that the contact angles are heterogeneously distributed on the grain surface. For example, the red (large contact angle) points and blue (small contact angle) points both appear in **Figs. 3a through 3c**, although the blue points dominate in **Fig. 3a** and red points dominate in **Fig. 3c**. However, the contact angles are not completely randomy istributed, but to some extent, they are spatially correlated. On the one hand, the regional agglomeration effect of the contact angle distribution is found in the results. In **Fig. 3a**, it is noteworthy that a small red (large contact angle) circle is attached to the grain surface in the middle part of the figure. In contrast, the other curves in this figure are mostly blue (small contact angle). A similar phenomenon is also observed in **Fig. 3b**. On the other hand, the images also demonstrate the local continuity of the contact angle. For a specific three-phase contact line, it is observed that the variation of the curve's color continues from warm color to cold color or vice versa. This finding indicates that the contact angle distribution is locally continuous when restricted to one three-phase contact line.

The statistical distributions of the local contact angle value are shown in **Figs. 3e and 3f**. The side length of the measurement box for each test is 600 voxels (9 mm). The number of measurement points for the three tests is 2,782,641, 241,509, and 221,187, respectively.

Downloaded from http://onepetro.org/SJ/article-pdf/30/01/180/4110338/spe-223938-pa.pdf/1 by Tsinghua University user on 15 May 2025

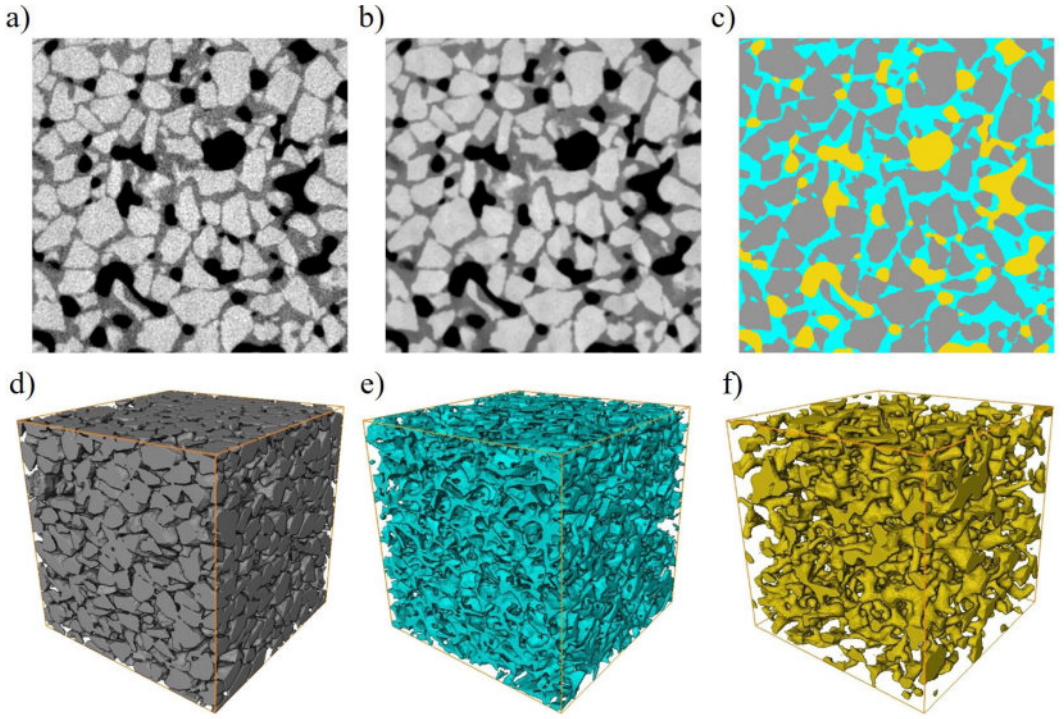

Fig. 2—Procedures for image processing and 3D visualization of the results: (a) raw image, (b) filtered image, (c) segmented image, (d) the sand grain, (e) the water phase in pore structure, and (f) the oil phase in pore structure.

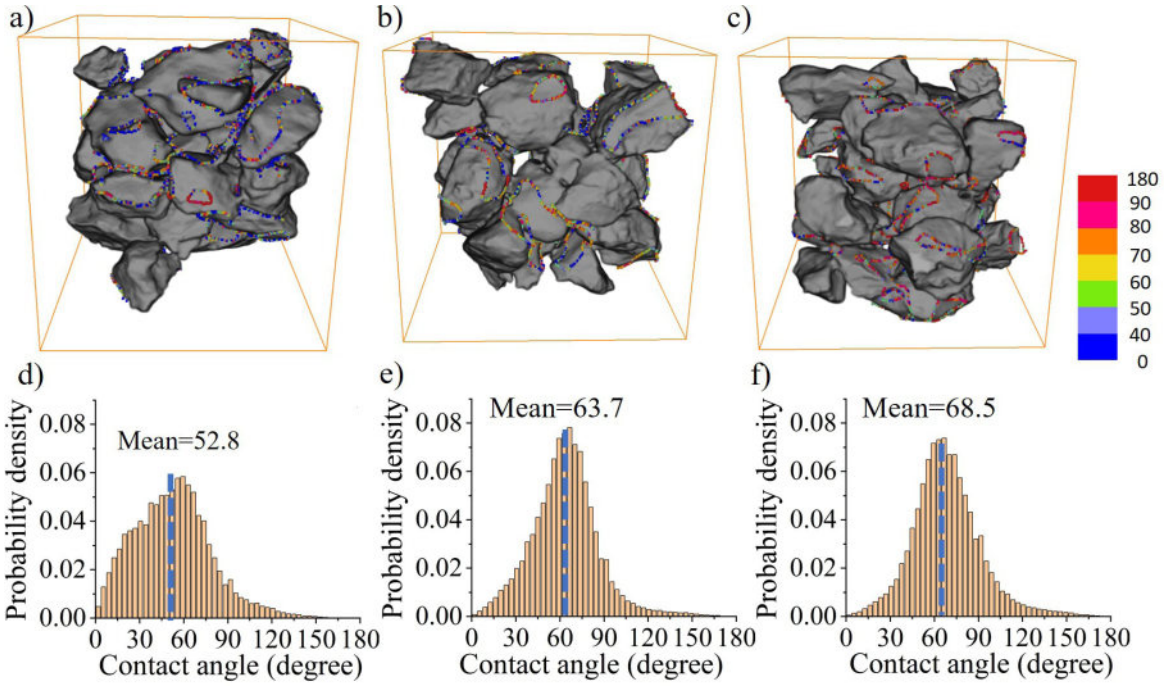

Fig. 3—Contact angle distribution within representative pore structures and the corresponding statistical distributions: (a) to (c) and (e) and (f) refer to testing of Sandpacks A, B, and C.

The mean value of distributions is 52.8, 63.7, and 68.5°, as annotated in each graph. After water-clay turbid treatment, the mean value of the contact angle increases. Higher clay content leads to a larger increment. The results indicate that water-clay turbid treatment is effective to alter the wettability of the sandpack to a less water-wet state. Besides, the contact angle distributions are more concentrated to their average value for Sandpacks B and C compared to Sandpack A. The kurtosis of the contact angle distribution is 0.47, 1.64 and 1.42 for Sandpacks A, B, and C. The results of kurtosis suggest that the heterogeneity associated with the statistical distribution of contact angle is diminished due to water-clay turbid treatment.

For traditional contact angle measurement, the contact angle hysteresis is defined as the difference between the value of the maximum (usually advancing angle) and the minimum (usually receding angle) measured contact angle. However, as seen in **Fig. 3** and previous

Downloaded from http://onepetro.org/SJ/article-pdf/30/01/180/4110338/spe-223938-pa.pdf/1 by Tsinghua University user on 15 May 2025

results of local contact angle (Singh et al. 2016), the entire distribution spans nearly from 0° to 180°. Thus, the largest difference of the measured contact angles cannot be used to characterize the contact angle hysteresis effect of our results. Therefore, we found the ten-fractile quantiles of each distribution in **Figs. 3e and 3f** and rearranged the data in **Fig. 4a**. In this graph, each colored block of the column stands for 10% sorted contact angle data. The separation line between two colored blocks indicates a ten-fractile quantile. For example, the first and ninth ten-fractile quantile for the Sandpack A test is 18.9° and 85.3° as marked in this graph. The data from the first ten-fractile quantile to the ninth ten-fractile quantile is the main component of the distribution, which reveals the main characteristic of the data distribution. In the 3D CT image, there is no precise criterion to determine whether the interface is advancing or receding. Thus, we cannot identify advancing and receding angles and further plot their distributions separately. From our experiment results, the measured contact angle distribution consisted of advancing angle, receding angle, and neutral angle between the two extreme states due to the water-oil coinjection. Therefore, we used the larger angle in the distribution to represent the advancing angle and the smaller angle to represent the receding angle. We chose the first and the ninth ten-fractile quantiles as the threshold. The selection of the threshold is not definite. The characteristic and evolution trend of contact angle hysteresis should be consistent with other proper thresholds. In **Fig. 4a**, it is noteworthy that the range of the main component becomes narrow after water-clay turbid treatment. The upper and lower boundary both rise, while the rising for lower boundary is more evident. We define the contact angle hysteresis as the difference between the ninth and first ten-fractile quantile:

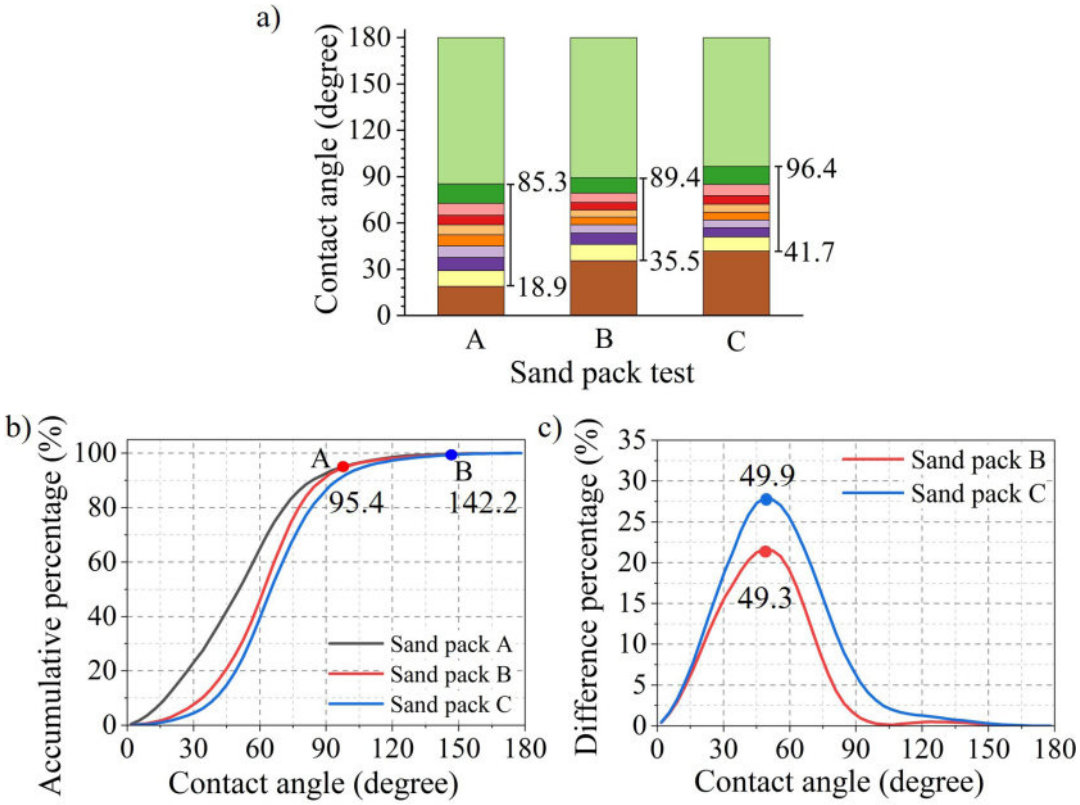

Fig. 4—Statistical distributions of the local contact angle: (a) ten-fractile-quantile distribution; (b) accumulative probability density distribution; and (c) difference of accumulative probability density distribution.

$$CA_h = Q_{10}^{9} - Q_{10}^{1}, \tag{1}$$

where CA_h denotes the contact angle hysteresis, the Q_{10}^{9} and Q_{10}^{1} refer to the ninth- and first ten-fractile quantiles. The calculated contact angle hysteresis is 65.4, 53.9, and 54.7° for Sandpacks A, B, and C, respectively. The results suggest that the water-clay turbid treatment can suppress the contact angle hysteresis effect.

To characterize the range of contact angle alteration due to the clay treatment, we plot accumulative probability density distribution curves of the contact angles in **Fig. 4b**, and the difference percentage curves in **Fig. 4c**. In **Fig. 4b**, the crossover point of Sandpack A test curve and Sandpack B test curve is marked as Point A, where the contact angle is 95.4°. The crossover point of Sandpack A test curve and Sandpack C test curve is marked as Point B, where the contact angle is 142.2°. The results indicate the alteration range of contact angle within the sandpacks is different. The range of contact angle alteration for Sandpack B test is from 0° to 95.4° while the range is from 0° to 142.2° for Sandpack C test. Higher clay content may lead to wider range contact angle alteration. In **Fig. 4c**, the red curve stands for the difference of accumulative probability density between Sandpack B and Sandpack A tests, and the blue curve stands for the difference of accumulative probability density between Sandpack C and Sandpack A tests. It is shown that the blue curve's distribution is wider than that of the red curve. The blue curve is always above the red curve. It suggests that compared with Sandpack B, not only the range of contact angle alteration is wider but also the amount of contact angle alteration data is larger for Sandpack C. Moreover, the peaks of the two curves appear in the similar position, where the contact angle is about 50°. It is noteworthy that this value is close to the mean contact angle of the Sandpack A test.

Wettability Evolution during Waterflooding. Figs. 5a through 5d show the contact angle distribution and its evolution within the pore structure of Sandpack A. It is noteworthy that the positions of three-phase contact lines on the grain surface are similar in the four images,

Downloaded from http://onepetro.org/SJ/article-pdf/30/01/180/4110338/spe-223938-pa.pdf/1 by Tsinghua University user on 15 May 2025

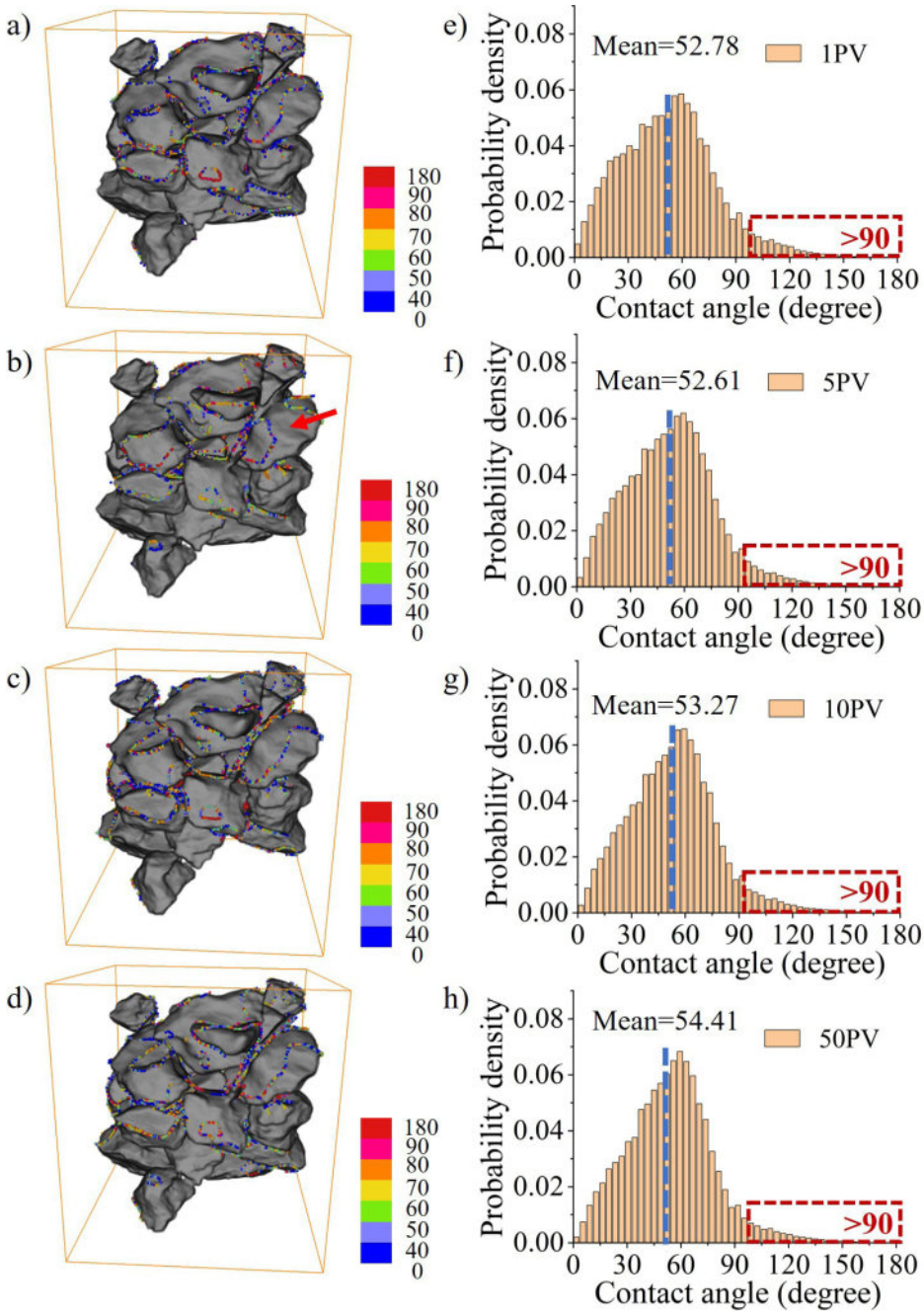

Fig. 5—Evolution of contact angle distribution within representative pore structures and the statistical distributions for the Sandpack A test: (a) to (d) refer to the waterflooding stages of 1 PV, 5 PV, 10 PV, and 50 PV, respectively; and (e) and (f) are the corresponding statistical distributions.

as shown in **Figs. 5a through 5d**. Only one contact line curve breaks into two curves, which is marked in **Fig. 5b**. The two curves merge into one three-phase contact line again in the following waterflooding stages, indicating that among different waterflooding stages, the distribution of the oil phase after water-oil coinjection is similar and the state of oil phase is relatively stable. Focused on the curves in the same position on the grain surface, we found a subtle variation of the curve's color, implying that the wettability change is not evident. Statistical distributions of contact angle during waterflooding are presented in **Figs. 5e through 5h**. The average contact angle and the portion whose value is larger than 90° are marked in the graphs. The position and the shape of the distributions are similar. The maximum difference of the average contact angle is only 1.8°. The average contact values (marked as the blue dashed line in the graph) of the four distributions are all located at the right of the peak value. The contact angle distribution shows that the variations of the wettability for the Sandpack A test are insignificant.

Fig. 6 illustrates the distribution and evolution of contact angles within the pore structure of Sandpack B. When compared to the Sandpack A test, significant disparities of three-phase contact line distributions on grain surfaces are observed across various waterflooding stages, as evident in **Figs. 6a through 6d**. Notably, the morphology of the three-phase contact lines on the marked sand grain undergoes significant changes. In **Fig. 6a**, the contact line appears as a small circle, which gradually grows larger in **Fig. 6b**. In **Figs. 6c and 6d**, the contact line further evolves, extending to neighboring grains and exhibiting an irregular morphology. These findings suggest substantial alterations in oil-phase distributions within the pore structure, likely influenced by changes in wettability. In addition,

Downloaded from http://onepetro.org/SJ/article-pdf/30/01/180/4110338/spe-223938-pa.pdf/1 by Tsinghua University user on 15 May 2025

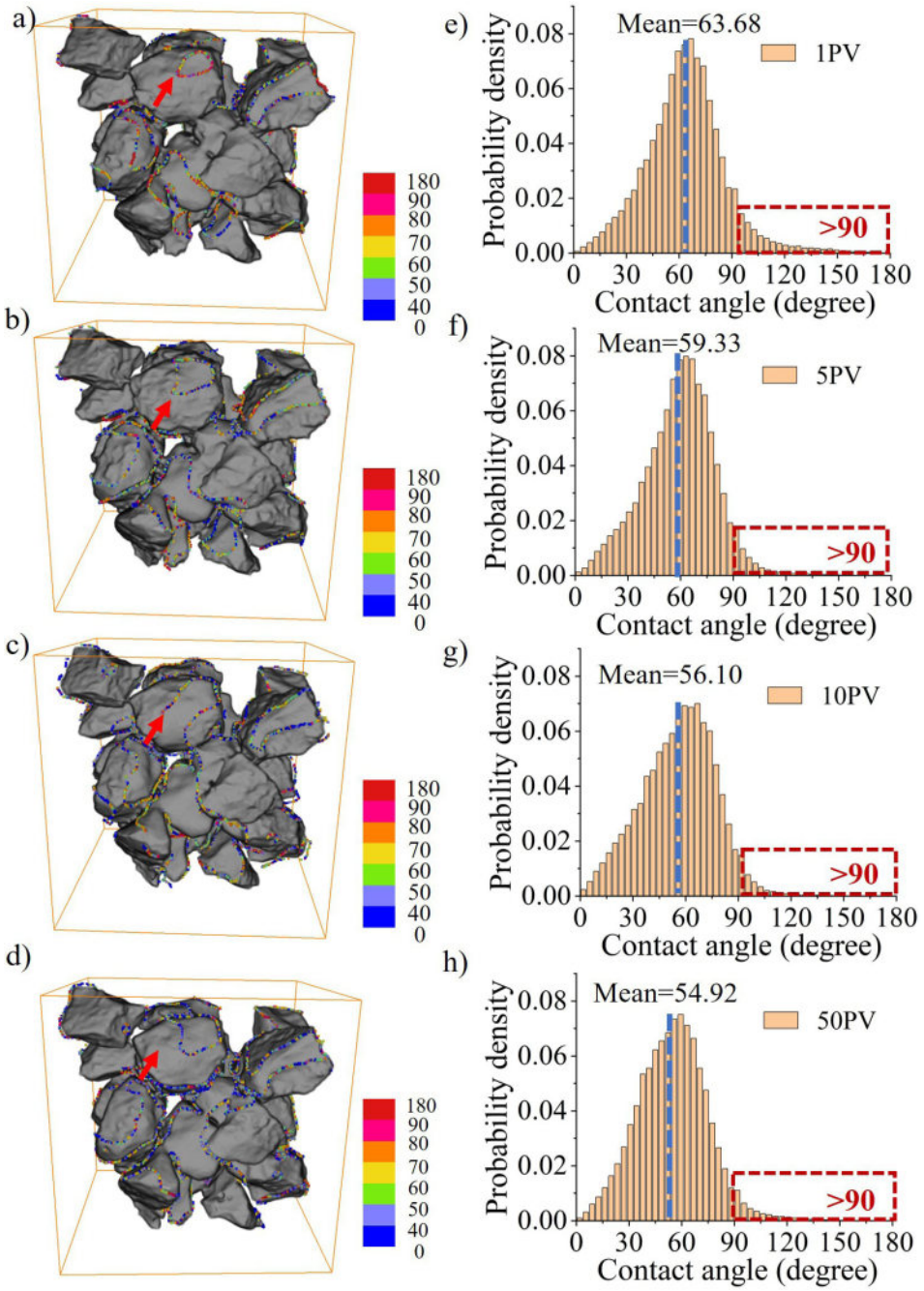

Fig. 6—Evolution of contact angle distribution within representative pore structures for Sandpack B and the statistical distributions: (a) to (d) refer to the waterflooding stages of 1 PV, 5 PV, 10 PV, and 50 PV, respectively; and (e) and (f) are the corresponding statistical distributions.

noticeable changes in the three-phase contact line's colors are observed. In **Fig. 6a**, numerous warm-colored data points are visible on the grain surface, with the three-phase contact line on the marked grain primarily composed of warm-colored points. As waterflooding progresses, however, the number of warm-colored data points decreases, as seen in **Figs. 6b through 6d**. In **Fig. 6d**, only a few warm-colored data points appear in the three-phase contact lines, randomly distributed across different three-phase contact lines. The average contact angle decreases from 63.68 to 54.92° after waterflooding, a significant decrease compared to the Sandpack A test, where the variation is only 1.8°. It is evident that the portion with contact angles larger than 90° (marked with a red box in the graph) becomes increasingly less significant during waterflooding. Furthermore, for the 1-PV test, the average contact angle (indicated by a blue dashed line in the graph) is located near the peak of the distribution. In contrast, at larger PV waterflooding stages, the average contact angle values are situated to the left of the peak. The results demonstrate that waterflooding is effective in modifying the wettability of the sandpack with clay content, shifting it toward a more water-wet state. Notably, the oil-wet portion of the sandpack (characterized by contact angles larger than 90°) is particularly sensitive to waterflooding. As a result, the sandpack becomes less oil-wet and increasingly water-wet, indicating a significant impact of waterflooding on wettability evolution.

The results of the Sandpack C test during waterflooding are presented in **Fig. 7**. The primary characteristics of contact angle distribution and wettability evolution exhibit similarities to the Sandpack B test. However, **Fig. 7** highlights a more significant variation in the position of three-phase contact lines. It is evident that the same three-phase contact lines cannot be traced consistently throughout **Figs. 7a**

Downloaded from http://onepetro.org/SJ/article-pdf/30/01/180/4110338/spe-223938-pa.pdf/1 by Tsinghua University user on 15 May 2025

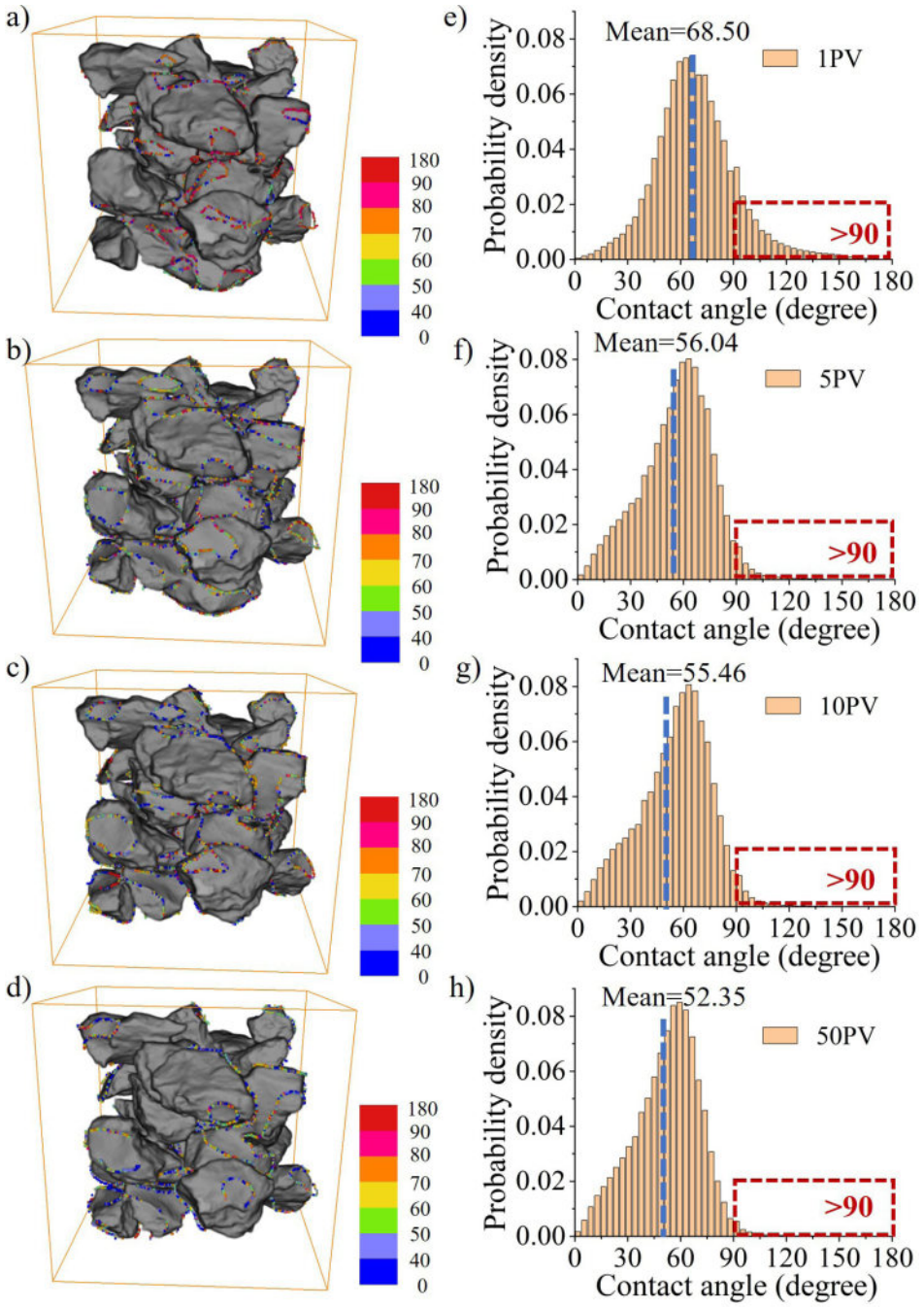

Fig. 7—Evolution of contact angle distribution within representative pore structures for Sandpack C and the statistical distributions: (a) to (d) refer to the waterflooding stages of 1 PV, 5 PV, 10 PV, and 50 PV, respectively; and (e) and (f) are the corresponding statistical distributions.

through 7d. This observation suggests a substantial difference in the distribution of the oil phase after water-oil coinjection, which is induced by the wettability evolution. Additionally, there is a notable alteration in the color of the three-phase contact lines. In **Fig. 7a**, the three-phase contact lines predominantly exhibit warm hues, whereas in **Figs. 7b through 7d**, they shift toward colder colors. The change of color indicates the wettability of Sandpack C changes to more water-wet. The statistical distributions of contact angles during waterflooding are depicted in **Figs. 7e through 7h**. The average contact angle decreases from 68.50° to 52.35° after waterflooding. Notably, the portion of contact angles larger than 90° is significantly reduced after the 5-PV waterflooding stage. In **Figs. 7g and 7h**, the proportion of contact angles exceeding 90° is negligible. Overall, the wettability evolution in the Sandpack C test is more pronounced compared to the Sandpack B test.

The evolution of the average contact angle across the three tests is graphically represented in **Fig. 8a**. For the Sandpack A test, minimal variations in the average contact angle are observed. However, when compared to the Sandpack A test, the Sandpacks B and C tests exhibit considerable decreases in the average contact angle with decreases of 8.76° and 16.15°, respectively. Notably, higher initial clay content leads to a more significant decrease in the average contact angle. Furthermore, the graph reveals that the majority of the decrease occurs primarily during the initial stages of waterflooding. Before 5 PV of waterflooding, the decrease measures 4.34° and 12.46°, accounting for 49.5% and 77.2% of the total average contact angle decrease, respectively. After 50 PV of waterflooding, the average contact angles of Sandpacks B and C settle below 55°, nearing the average contact angle of the Sandpack A test. It is noted that since 5

Downloaded from http://onepetro.org/SJ/article-pdf/30/01/180/4110338/spe-223938-pa.pdf/1 by Tsinghua University user on 15 May 2025

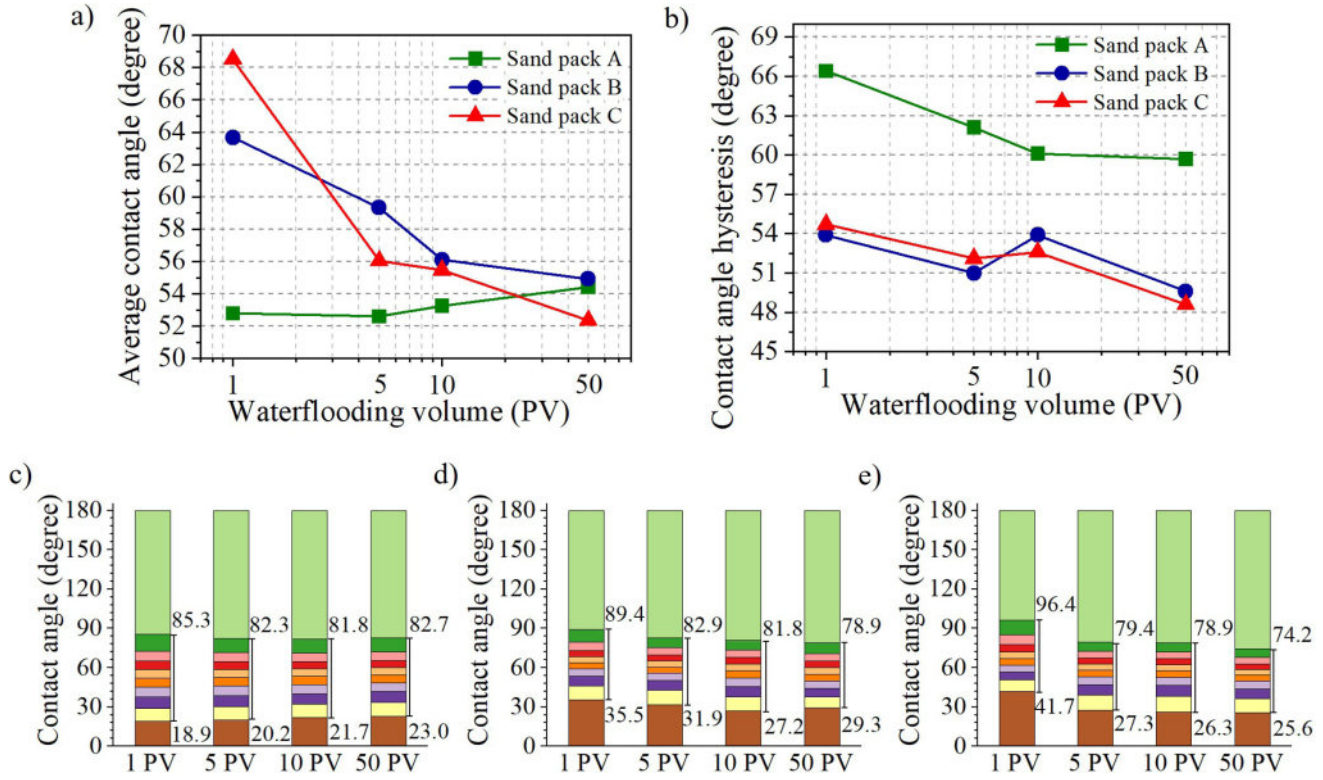

Fig. 8—Wettability characteristics evolution during waterflooding: (a) evolution of average contact angle; (b) evolution of contact angle hysteresis; and (c) to (e) evolution of ten-fractile quantiles for contact angle distributions.

PV waterflooding, the mean contact angle for Sandpack C was smaller than that of Sandpack B. Although the initial clay content of Sandpack C was highest and the same experimental method was applied, it was not definite that the clay content for Sandpack C was still higher than that of Sandpack B after waterflooding. Clay deposition in pore structure was heterogeneous, and its transportation may not only be dependent on the initial clay content. The sandpack models used in the experiment had similar porosity and permeability. However, we cannot ensure that the pore structures of the sandpack models were identical. The clay content decreased during waterflooding, but the exact value of clay content during waterflooding cannot be precisely controlled under the current experimental condition. The mean contact angle for Sandpacks B and C decreases rapidly in the initial stage of waterflooding and then slows down. It may be induced by the rapid decrease of clay in the early stage. During the Sandpack B and C tests, we observed that the liquid released from the sandpack was turbid at first and then became clear as the waterflooding volume increased. Sandpack A responded differently because there was no clay in Sandpack A. The impact of clay is not effective, and the variation of mean contact angle was not significant. In addition, according to the evolution trend of mean contact angle, we infer that the change will stop after a certain point. When the clay in the sandpack reaches its residual content, the clay content will not change with waterflooding. The contact angle or the wettability ceases to evolve.

Figs. 8c through 8e illustrate the evolution of ten-fractile quantiles for contact angle distributions throughout various tests. Specifically, **Figs. 8c through 8e** depict the results from the Sandpacks A, B, and C tests, respectively. In the Sandpack A test **(Fig. 8c)**, the ten-fractile quantiles exhibit minimal variation. However, in the Sandpacks B and C tests, a notable trend emerges: The main component of the distribution (encompassing the range from the first to the ninth ten-fractile quantile) shifts downward during waterflooding. This shift is asymmetric, with the upper boundary decreasing by 10.5° for the Sandpack B test and 22.2° for the Sandpack C test, while the lower boundary decreases by 6.2° and 16.1°, respectively. The contact angle hysteresis, defined in Eq. 1, represents the difference between the upper and lower boundaries of the distribution's main component. Contact hysteresis is calculated based on **Figs. 8c through 8e** and plotted in **Fig. 8b**. The results illustrate that the hysteresis curve for the Sandpack A test remains consistently above the curves for the Sandpacks B and C tests, indicating a more significant hysteresis effect in Sandpack A. During waterflooding, all three tests show a decrease in hysteresis, as evidenced by the descending curves in **Fig. 8b**. Notably, the curves for Sandpacks B and C overlap, indicating a similar evolution trend. The nonmonotonic trend of contact angle hysteresis for Sandpacks B and C is explained using **Fig. S-5** in the Supplementary Material.

Wettability REV Size and Wettability Heterogeneity. REV is a fundamental concept for the investigation of fluid flow in porous media that bridges the gap between microscale mechanism and Darcy scale flow phenomenon. In previous sections, it has been proved that the contact angle distribution within the pore structure is highly heterogeneous. It is necessary to figure out the REV size of wettability and its evolution during waterflooding.

First, the REV size of porosity in the sandpacks is determined. Porosity of various-sized subvolume cube is calculated from the 3D CT images. Porosity is calculated by the following equation:

$$\varphi = \frac{N_{\text{pore}}}{N_{\text{total}}}, \tag{2}$$

Downloaded from http://onepetro.org/SJ/article-pdf/30/01/180/4110338/spe-223938-pa.pdf/1 by Tsinghua University user on 15 May 2025

where φ is the porosity of a subvolume, N_{pore} is the number of voxels belonging to pore space, and N_{total} is the number of total voxels in the subvolume. For a given subvolume size, 20 randomly selected subvolumes from the 3D CT image undergo porosity calculations, with the results plotted in **Fig. S-2a** in the Supplementary Material. Simultaneously, the standard deviation of the porosity data from these ten subvolumes of the same size is calculated and presented in **Fig. S-2b**.

Fig. S-2a shows that the porosity rapidly converges to a specific value as the size of the subvolume increases. Notably, the trend of Sandpacks A, B, and C tests are consistent, suggesting comparable REV sizes among the three sandpacks. **Fig. S-2b** exhibits a significant decrease in standard deviation as the increase of subvolume size. In this study, the porosity with a standard deviation no greater than 2% is set as the representative porosity for the rock, and the corresponding size of the subvolume cube is the REV size for porosity:

$$\text{std}_p \leq 0.02\varphi, \tag{3}$$

where std_p stands for the standard deviation of porosities of given sized subvolume cubes. Based on this criterion, the REV sizes for Sandpacks A, B, and C are determined to be 52.6 mm³, 46.1 mm³, and 43.4 mm³, respectively. Correspondingly, the side length of the subvolume cube ranges from 3.51 mm to 3.75 mm. Compared to the dimensions of the sandpack column (15-mm diameter and 80-mm height) and the CT scanning field of view (15-mm width and 15-mm height), the REV size is sufficiently small. Furthermore, the porosity REV sizes of Sandpacks A, B, and C are remarkably similar. The findings about porosity REV lay the foundation for subsequent analyses of wettability REV size and wettability heterogeneity.

The method for wettability REV estimation is similar to porosity REV estimation. First, average contact angle is determined in various-sized subvolume cubes:

$$\overline{\theta} = \frac{1}{N}\sum_{i=1}^{N}\theta_i, \tag{4}$$

where $\overline{\theta}$ refers to the average contact angle of a given sized subvolume cube, N refers to the number of contact angle data points in the subvolume cube, and θ_i refers to the contact angle value of each data point. For a given subvolume size, 20 randomly selected subvolumes from the 3D CT image undergo average contact angle calculations, and the standard deviation of the 20 average contact angles is also calculated. The variation of average contact angle and standard deviation as the subvolume increases in size are plotted in **Fig. 9**.

Figs. 9a through 9c present the variation of average contact angle as the increase of subvolume size for Sandpacks A, B, and C. Scatters with different colors refer to the results of different waterflooding stages. It is shown that all scatters are almost overlapped in **Fig. 9a**. While in **Figs. 9b and 9c**, different-colored scatters converge to different values. This is consistent with the previous findings: The variation of average contact angle for the Sandpack A test is negligible, while the variation of average contact angle for Sandpacks B and C is considerable. **Figs. 9d and 9e** present the variation of standard deviation as the increase of subvolume size for Sandpacks A, B, and C. The black, red, blue, and green scatters refer to 1 PV, 5 PV, 10 PV, and 50 PV waterflooding stages, respectively. Overall, the standard deviation decreases for all tests as seen in the three graphs. During the waterflooding process, the distribution of scatters for different waterflooding stages is different, indicating the variation of the wettability REV size. In **Fig. 9d**, the correlation of waterflooding volume and standard deviation is not very clear. The red scatters are in the upper part among the scatters, and the blue, green, and black scatters are overlapped in the graph, implying that for Sandpack A, the wettability REV size is the largest at the 5-PV waterflooding stage. While in **Figs. 9e and 9f** a consistent pattern is observed, the black and green scatters are distributed in the upper and lower parts among the scatters, and the red and blue scatters are between the black and green scatters, indicating that for Sandpacks B and C, the REV size is largest at the beginning of the waterflooding and smallest at the end of the waterflooding. This is to say that the REV size decreases as the waterflooding goes on.

To determine wettability REV size, the below criterion is applied:

$$\text{std}_{ca} \leq 0.02\overline{\theta}, \tag{5}$$

where std_{ca} stands for the standard deviation of average contact angles of given sized subvolume cubes. It should be noted that this criterion and the coefficient 0.02 are not unique methods for REV estimation. With other reasonable criteria, the exact REV size may be different, but the overall evolution trend of the REV size should be consistent.

Fig. 10 shows the evolution of wettability REV size during waterflooding tests. At the 1-PV waterflooding stage, the wettability REV size of the Sandpack C test is larger than others. In the following waterflooding stages, the wettability REV size of the Sandpack A test is always larger than that of the Sandpacks B and C tests. Moreover, the Sandpack A test shows a trend of increase and then decrease in wettability REV size, while the Sandpacks B and C tests demonstrate a continuous decline of wettability REV size during the waterflooding process. It is noteworthy that the REV size of Sandpack B is almost the same as the Sandpack A test at the 1-PV stage. Due to the monotonic descent trend of the curve for the Sandpack B test, it is very likely the REV size of Sandpack B is larger than that of Sandpack A before waterflooding. Throughout the waterflooding tests, the decrease of wettability REV size is about 60% for the Sandpack C test and 50% for the Sandpack B test. At the end of the test, the wettability REV sizes of Sandpacks B and C are very close. The wettability REV size of the Sandpack A test is slightly larger than that of the Sandpacks B and C tests. The alteration of wettability REV is intrinsically controlled by the heterogeneity of contact angle spatial distribution, which is influenced by the waterflooding process in our study. The evolution of wettability REV size highlights the impacts of clay content and waterflooding on the contact angle spatial distribution, especially its heterogeneity. In addition, the relationship of the contact angle hysteresis, the distribution heterogeneity of contact angle, and the wettability REV size is explained by **Fig. S-6** in the Supplementary Material.

Mechanism of Sandpack Wettability Evolution. Roughness is a prime factor that influences the contact angle. According to previous studies, roughness can enhance the wetting tendency of the surface (Quéré 2008). On a water-wet surface, the appearance of roughness can make the surface more water-wet. Similarly, on an oil-wet surface, roughness intensifies its oil-wet state. In addition, the hysteresis effect of contact angle is enhanced on rough surface compared to smooth surface. It is noteworthy that the roughness does not alter the intrinsic wettability of the wetting system. The pining effect of the three-phase contact line at the local microstructure is the main mechanism for wettability alteration induced by roughness. In our experiment, we keep all conditions unchanged except for the clay content of the sandpack. The results show that the wettability state alters as we change the clay content. Moreover, the wettability state of the clay sandpacks varies during the waterflooding process. The variation of wettability is probably induced by the variation of the

Downloaded from http://onepetro.org/SJ/article-pdf/30/01/180/4110338/spe-223938-pa.pdf/1 by Tsinghua University user on 15 May 2025

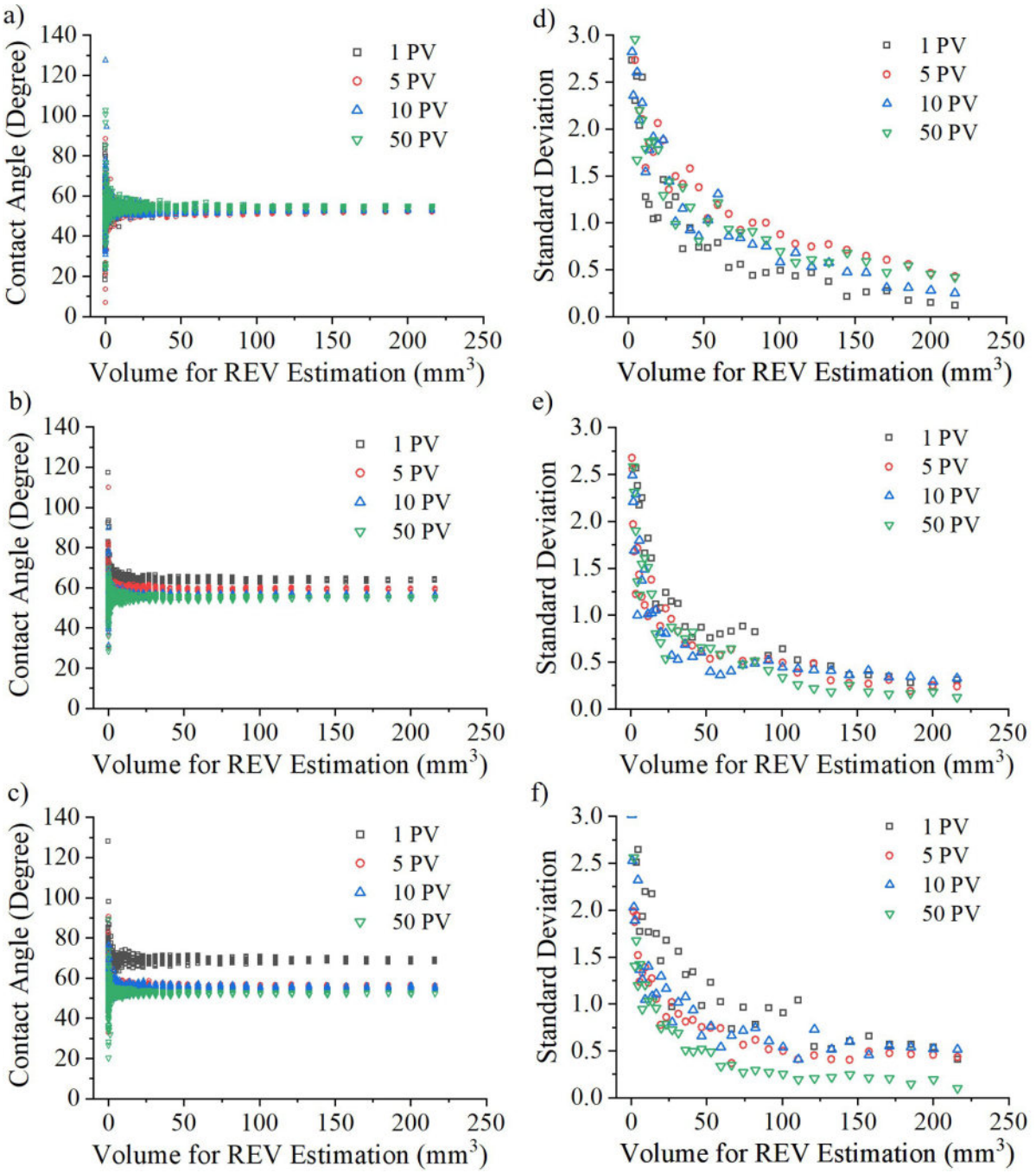

Fig. 9—Wettability REV estimation: (a) to (c) variation of average contact angle as the increase of box volume for Sandpacks A, B, and C tests; (d) and (f) variation of standard deviation as the increase of box volume for Sandpacks A, B, and C tests.

clay content in the sandpack. Based on these findings, we infer that the roughness of the sand grain and the clay content are the main factors that control the wettability in our study. In this section, we propose a simplified physical model to explain the wettability evolution phenomenon during long-term waterflooding.

The key points of our physical model are surface roughness and clay deposition patterns. It is assumed that the surface roughness of sand grains consists of multiple layers, which intends to capture the complexity of a natural rough surface, for example, the surface with three layers of rough structure (Type A), as shown in **Fig. 11**. With more layers of roughness, the enhancement of the wetting state and the contact angle hysteresis effect is more significant. When the clay is added to the sandpack, it will deposit on the rough grain surface and fill the concavity. Consequently, the roughness of the surface will reduce. If the clay content is sufficient to fully fill the concavity of the rough surface, the surface becomes smooth, and the wetting behavior is mainly controlled by the clay, as demonstrated in **Fig. 11** for Type B. For the Type B surface, the mean contact angle is close to the contact angle of clay, and the contact angle hysteresis is relatively small. Due to the complicated pore structure and clay deposition process, partially filled rough surfaces are also considered, such as Types C and D in **Fig. 11**. The difference between Type C and Type D is the clay-covered surface ratio. For a Type C surface, more clay area is exposed to liquids, while for a Type D surface, more sand surface area is exposed to liquids. Meanwhile, the Type D surface keeps more rough structure of the sand grain compared to Type B and Type C surfaces. The layers of roughness structure for Types A to D are 3, 0, 1, and 2, respectively. The four types of surfaces coexist in the sandpack with one of them taking up the majority. The ratio of each type of surface

Downloaded from http://onepetro.org/SJ/article-pdf/30/01/180/4110338/spe-223938-pa.pdf/1 by Tsinghua University user on 15 May 2025

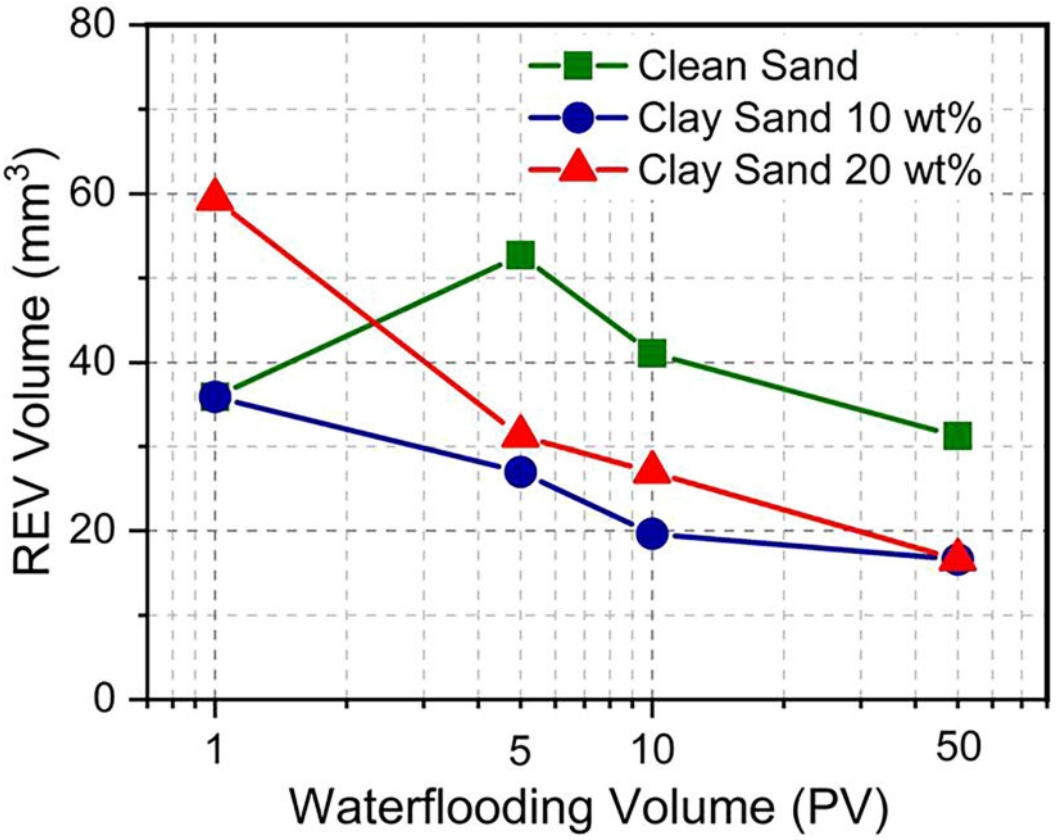

Fig. 10—Evolution of wettability REV size during waterflooding tests.

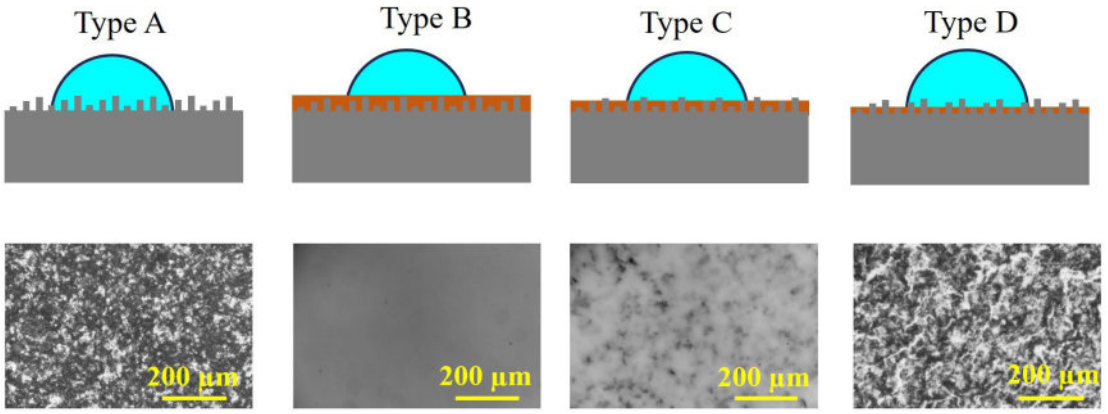

Fig. 11—Typical clay deposition patterns on rough surface. The first row represents the physical models of Types A to D, and the second row is the real rough glass plate model covered with various clay content, corresponding to the first row.

alters continuously as the experimental condition changes, such as by adding clay or through waterflooding. The wettability characteristics of the sandpack, including mean contact angle, contact angle hysteresis, and wettability heterogeneity, are controlled by the evolution of the four surface types, which represent the impacts of surface roughness and clay deposition patterns.

Because Type A is the only surface type in the Sandpack A test, there is no variation in surface roughness or clay deposition pattern during the waterflooding process. Thus, the mean contact angle is almost unchanged during the waterflooding test. It is noteworthy that contact angle hysteresis and the wettability heterogeneity vary slightly. This may be induced by the trapped oil in the concavity (AlRatrout et al. 2018; Schmatz et al. 2015). Oil in the concavity of the rough surface can influence the chemical heterogeneity and thus impact the contact angle. In Sandpacks B and C, after the water-clay turbid treatment, clay deposition pattern changes from Type A to a mixture of Types B, C, and D, while Type B is the major deposition pattern. Because Types B, C, and D surfaces are less rough compared with the Type A surface, the effect of contact angle hysteresis and the wetting enhancement become weak. For the higher clay content test, the ratio of Type B surface is higher. Therefore, the contact angle increase is larger for Sandpack C. During the waterflooding process, some of the clay deposited on the grain surface may be washed away. Accordingly, the surface types and its ratio evolve continuously. The ratio of Type B surface further decreases and transits into Type C or Type D surface. The overall roughness of the sandpack system increases. Thus, the wetting enhancement effect induced by roughness is strengthened, and the average contact angle decreases. In addition,

Downloaded from http://onepetro.org/SJ/article-pdf/30/01/180/4110338/spe-223938-pa.pdf/1 by Tsinghua University user on 15 May 2025

waterflooding is used to make the clay deposition more homogeneous. Consequently, the size of wettability REV becomes smaller during the waterflooding process, and the contact angle spatial distribution becomes more homogeneous.

A supplemental experiment was carried out to further validate the mechanism of wettability evolution associated with roughness and clay deposition. We used rough quartz glass plates to mimic the rough surface of sand grain. Water-clay turbids with clay mass ratios of 10 wt%, 15 wt%, and 20 wt% were prepared to simulate the water-clay turbid treatment. Different clay deposition patterns are achieved by dropping different water-clay turbid onto the rough glass and waiting for water to evaporate. The second row of **Fig. 11** shows the microscopic images of rough glass surface treated with water and 20 wt%, 15 wt%, and 10 wt% water-clay turbid. The four rough glass surfaces correspond to the four types of surfaces in the first row, respectively. As shown in **Fig. 11**, the rough glass surface consists of many layers of rough structure with different heights. Although it is impossible to fabricate the same rough structure as the sand grain, the rough glass plate captures the key features of the rough grain surface. The Type B rough glass surface is fully covered with clay. The surface becomes smooth and no protrusion can be observed. For the Type C rough glass surface, clay covers most of the rough structure, but some peaks of the rough structure are exposed to air, while for the Type D rough glass surface, clay only fills the valley of the rough structure. Most rough structures are exposed to the air. The contact angles were then measured with the four treated types of rough glass plates using the experimental liquids mentioned in the section "Materials." Contact angles were measured by a drop shape analyzer (DSA25, Krüss, Germany) using the captive bubble method and Young-Laplace fitting.

The measurement results are summarized in **Fig. 12**. As a benchmark, the contact angle on clean smooth glass surface is also measured as Type E. In this figure, the oil is shown as the black bubble; the glass plate is over the bubble, and the brine occupies the other area below the glass plate. For Types B, C, and D tests, the brine is a little turbid because a small portion of clay on the rough surface disperses in the brine. The morphology of the captive bubbles indicates that all the testing systems are water-wet. A clean rough (Type A) surface shows the strongest water affinity with an average contact angle of 27.1°. And the average contact angle of clean smooth (Type E) surface is 39.8°. This result confirms the wetting enhancement effects of surface roughness. The contact angle of Types B, C, and D surfaces are 52.8°, 46.6°, and 40.0°, respectively. Because the Type B surface is fully covered with clay, the contact angle can be used as the contact angle of clay. The results also indicate that as the clay content decreases, the average contact angle decreases, which is consistent with the pore scale contact angle evolution results. Besides, as demonstrated in **Fig. 11**, the structure morphology of the rough surface is controlled by the clay content deposited on it. More rough structures appear due to the decrease in clay content. It further validates the analysis of the wettability evolution mechanism in our physical model.

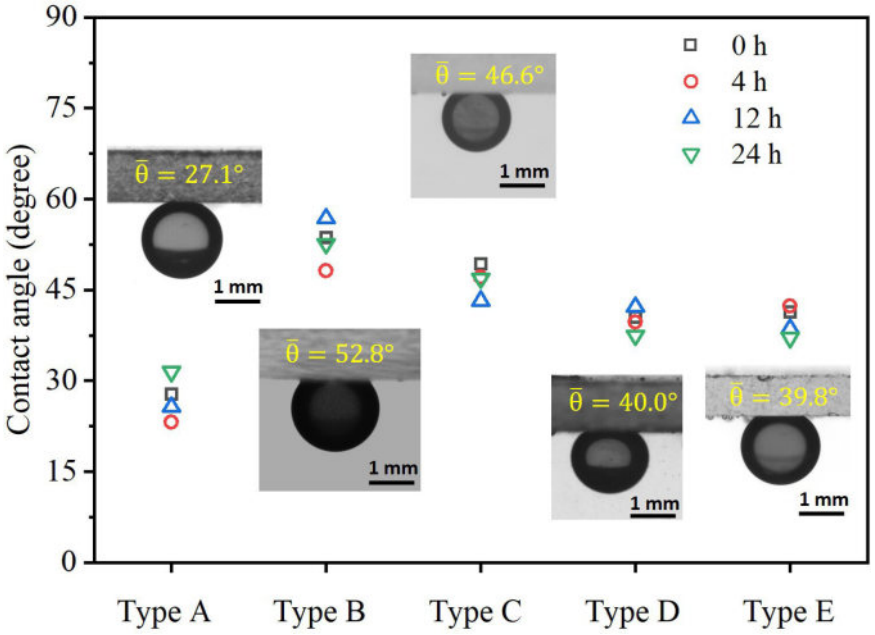

Fig. 12—Results of contact angle measurement on rough glass plate covered with various clay contents.

The evolution from Type B to Type C and then Type D represented the dynamic transition of the surface types during waterflooding. However, the dynamic transition of surface type is our deduction based on the experimental process and results. We admit that the current experimental equipment has limited imaging resolution; therefore, we cannot detect the nanoscale roughness or fine clay deposition patterns. To observe such phenomenon, nano-CT is required, but it brings new challenges about the trade-off between the field of view and the resolution, which is a long-standing problem. For example, assuming that the characteristic length of the irregular roughness structure is 0.1 μm, to capture such structure, the field of view for CT imaging is usually less than 200 μm. The main object of this study is to characterize the wettability evolution of sandpack with clay content during long-term waterflooding. To achieve this goal, we applied micro-CT to detect the interfaces between liquids and solids and further measure the contact angles. When nano-CT is used, it will be impossible to obtain sufficient three-phase contact lines for contact angle measurements due to the small field of view. The characterization of nanoscale roughness and clay deposition patterns is important for the study of the wettability behavior. In our future work, we plan to experimentally characterize the impacts of nanoscale surface roughness and clay deposition on the variation of contact angle. We use the new experiment results to validate our contact angle model.

Discussion

Because the evolution of contact angle is induced by the change of clay content, there should be critical clay contents for the starting and ending of contact angle evolution. If the clay content is high enough to cover all the rough structure, the contact angle will not change

Downloaded from http://onepetro.org/SJ/article-pdf/30/01/180/4110338/spe-223938-pa.pdf/1 by Tsinghua University user on 15 May 2025

through waterflooding unless the deposition height decreases further to expose rough structure. This is the critical deposition height (H_0) or clay content (C_0). Below clay content C_0, the clay content and deposition height decrease with the waterflooding process. The roughness feature and chemical heterogeneity of the surface vary continuously. Accordingly, the contact angle changes noticeably as waterflooding. Through the process of waterflooding, the deposition height and clay content eventually decrease to its residual value (H_r and C_r). After that, the roughness feature and chemical heterogeneity of the surface will not change as waterflooding. The change of contact angle finally stops. A point of diminishing returns in terms of wettability changes may also exist because mean contact angle decreases sharply in the initial stage of the waterflooding and then slows down.

It is noted that the change of mean contact angle was small for Sandpack A, while the variation of contact angle hysteresis and wettability REV size was noticeable. Oil film adhered to the rough grain surface could be the underlying cause. The oil can fully contact the rough surface even at the small concavity and thus adhere to the rough area. Mean contact angle, contact angle hysteresis, and wettability REV size describe the wettability from different views. Contact angle hysteresis measures the difference between large and small contact angles. It is sensitive to the extreme values of the measured contact angle. The appearance of oil film changes the extreme value of contact angles and results in the variation of contact angle hysteresis. Wettability REV size measures the heterogeneity of contact angle spatial distribution within pore structure. It is sensitive to the spatial distribution mode (homogeneous or heterogeneous) of contact angles. The appearance of oil film and its evolution lead to the change of contact angle value at a specific position. The homogeneity changes regarding contact angle spatial distribution, resulting in the variation of wettability REV size. Because the sandpack is weak water-wet, the amount of oil film is small. The impacts of a few changed values on mean contact angle are negligible due to the vast measurement points of contact angle. Oil films may exist in all sandpack tests and contribute to the wettability evolution. The amount and spatial distribution could impact the mean contact angle, contact angle hysteresis, and wettability REV size. To integrate the effects of oil films into the model, the adhesion behavior of oil films should be studied carefully, and the influence of waterflooding on the occurrence of oil films should be assessed. Based on the Wenzel and Cassie model, the influence of roughness can be assessed. We can treat the effects of clay and oil film as chemical heterogeneity in the model, qualifying them by means of their area fractions and intrinsic contact angles. Combined with the mathematical description of clay deposition variation and oil film evolution, a comprehensive wettability model could be established.

Kaolinite was used as clay in the experiment. There are many other kinds of clays in reservoir rocks such as montmorillonite, illite, and pyrophyllite. They have different physical or chemical features and may result in various responses to waterflooding. For example, smectites are featured by smaller particle sizes and huge specific surface area. Under this condition, the adsorption effect of clay is noteworthy because adsorption of polar compounds from crude oil may also influence wettability significantly. Moreover, the swelling of smectites may block narrow throats of pore structure and modify the flow field, resulting in the enhancement of grain surface erosion around the preferential flow path. Thus, the heterogeneity of contact angle spatial distribution could be more evident as waterflooding. Besides, clays could be mixed-deposited in the pore structure. The wettability evolution may respond differently in this condition. It is also possible that there are unknown complex mechanisms that control the wettability evolution in reservoirs with mixed clay compositions compared with single clay composition condition. Limited by the length of the manuscript, we cannot carry out all tests with various clays and summarize the differences, while it is meaningful and important for further investigation.

In previous investigations about the impacts of wettability on water-oil displacement, the wettability state of the porous media is usually treated as homogeneous and static. Our study has shown that the wettability state of rock undergoes a continuous evolution. For the study of enhanced oil recovery, these changes could be used as the constraint conditions to explore the water-oil displacement efficiency, the trapping mechanism of oil, and the mobilization of trapped oil. It can also be used to establish wettability evolution models, incorporate with a multiphase flow simulator, and assess the impacts of wettability manipulation methods on enhanced oil recovery. In more complex reservoirs, the clay content and its deposition homogeneity may be different across geological formations. In the formation where the clay content is high and the deposition is homogeneous, the wettability changes could be significant after long-term waterflooding. In addition, there are many geological formations with various permeabilities in the subsurface. A preferential flow path usually appears in formations with high permeability. Around the preferential flow path, the rock goes through intensive waterflooding, and the clay deposition pattern alters significantly. There may be evident wettability alteration around the preferential flow path compared with adjacent formations. Consequently, wettability contrast could appear between formations and may influence the liquid exchange behavior across formations. We cannot definitively say whether this phenomenon is beneficial or detrimental to improving oil recovery. Nevertheless, it is a potential factor that impacts oilfield development and is worthy of further investigation. There are many factors or mechanisms that influence wettability, such as lithologies, mineral compositions, flow regimes, liquid property, and rock permeability. To accurately predict the wettability behaviors, comprehensive methods or models are needed. This paper is a fundamental and preliminary study, and we only intend to characterize the wettability evolution induced by clay content variation during long-term waterflooding. We used a simplified experimental setup to eliminate the impacts of other factors so that we can focus on our object. Our research scheme begins with simple scenarios and then progresses to tackling complex problems. Application to reservoir-condition scenarios is our final goal, while it is impossible to solve all the problems associated with nature reservoir wettability in one investigation. Significant effects and cooperation from the community are required to realize the accurate prediction of the wettability behaviors in natural reservoirs. Nevertheless, the findings and mechanism reported in this paper can serve as the basis for further comprehensive methods or models of wettability prediction.

Conclusions

In this study, we explored the wettability evolution behavior of sandpacks with various clay contents during long-term waterflooding experiments. By in-situ CT imaging and local contact angle measurements, the contact angle distribution and its evolution during waterflooding were obtained. Contact angle distribution instead of a single wettability index provided a more detailed description of the wetting state in sandpacks. The wettability evolution was quantitatively characterized by the mean contact angle, contact angle hysteresis, and wettability REV size. Moreover, a physical model considering surface roughness and clay deposition patterns was proposed to reveal the mechanism of wettability evolution. The findings of this study provide fundamental knowledge for further wettability model development and multiphase flow investigation. The major points are listed below:

1. The contact angle measurements at pore scale demonstrated that the contact angles are heterogeneously distributed while locally continuous on the grain surface. The water-clay turbid treatment is effective to alter the wettability state of the sandpack to a less water-wet state. Higher clay content leads to more significate wettability alteration. In addition, the contact angle hysteresis effect is diminished due to the clay deposition.
2. During the waterflooding process, the mean contact angle of Sandpack A does not vary significantly, while a sharp decrease in the mean contact angle of Sandpacks B and C is observed. The major decrease occurs in the early stage of the waterflooding. The contact

Downloaded from http://onepetro.org/SJ/article-pdf/30/01/180/4110338/spe-223938-pa.pdf/1 by Tsinghua University user on 15 May 2025

angle hysteresis effect is suppressed for all groups. The spatial distribution of contact angles becomes less heterogeneous, and this phenomenon is more evident in Sandpacks B and C.

3. The mechanism of wettability evolution is revealed by a physical model considering clay deposition patterns and sand grain surface roughness. Water-clay turbid treatment and waterflooding influence the ratio of four clay deposition patterns and thereby change the overall roughness of the sandpack system. The evolution of mean contact angle and contact angle hysteresis are mainly controlled by the wetting enhancement effect associated with surface roughness. The wettability REV size is influenced by the homogeneity of clay deposition in the pore space. The surface chemical heterogeneity associated with oil film and clay may also impact the behavior of wettability evolution.

It is noteworthy that this work is a primary study focusing on the influence of clay content on wettability. Due to the variety and complexity of nature reservoir rocks, such as clay type, pore structure, brine composition, and permeability, the mechanism of wettability evolution requires further comprehensive research.

Acknowledgments

This work is financially supported by the NSF grant of China (Nos. 12432013 and 12272207) and the National Key Research and Development Program of China (No. 2019YFA0708704).

References

Alnoush, W., Shaat, A., and Alyafei, N. 2022. What Is the Optimum Wettability for Oil Recovery Through Waterflooding? Paper presented at the SPE Conference at Oman Petroleum & Energy Show, Muscat, Oman, 21−23 March. https://doi.org/10.2118/200232-MS.

AlRatrout, A., Blunt, M. J., and Bijeljic, B. 2018. Wettability in Complex Porous Materials, the Mixed-Wet State, and Its Relationship to Surface Roughness. *Proc Natl Acad Sci U S A* **115** (36): 8901–8906. https://doi.org/10.1073/pnas.1803734115.

AlRatrout, A., Raeini, A. Q., Bijeljic, B. et al. 2017. Automatic Measurement of Contact Angle in Pore-Space Images. *Adv Water Resour* **109**: 158–169. https://doi.org/10.1016/j.advwatres.2017.07.018.

Amott, E. 1959. Observations Relating to the Wettability of Porous Rock. *Trans AIME* **216** (1): 156–162. https://doi.org/10.2118/1167-G.

Anderson, W. G. 1986. Wettability Literature Survey- Part 2: Wettability Measurement. *J Petrol Technol* **38** (11): 1246–1262. https://doi.org/10.2118/13933-PA.

Andrew, M., Bijeljic, B., and Blunt, M. J. 2014. Pore-Scale Contact Angle Measurements at Reservoir Conditions Using X-Ray Microtomography. *Adv Water Resour* **68**: 24–31. https://doi.org/10.1016/j.advwatres.2014.02.014.

Armstrong, R. T., Sun, C., Mostaghimi, P. et al. 2021. Multiscale Characterization of Wettability in Porous Media. *Transp Porous Med* **140** (1): 215–240. https://doi.org/10.1007/s11242-021-01615-0.

Arshadi, M., Gesho, M., Qin, T. et al. 2020. Impact of Mineralogy and Wettability on Pore-Scale Displacement of NAPLs in Heterogeneous Porous Media. *J Contam Hydrol* **230**: 103599. https://doi.org/10.1016/j.jconhyd.2020.103599.

Arzilli, F., Cilona, A., Mancini, L. et al. 2016. Using Synchrotron X-Ray Microtomography to Characterize the Pore Network of Reservoir Rocks: A Case Study on Carbonates. *Adv Water Resour* **95**: 254–263. https://doi.org/10.1016/j.advwatres.2015.07.016.

Bai, Y., Hou, J., Liu, Y. et al. 2022. Energy-Consumption Calculation and Optimization Method of Integrated System of Injection-Reservoir-Production in High Water-Cut Reservoir. *Energy***239** (6). https://doi.org/10.1016/j.energy.2021.121961.

Belhaj, A. F., Fakir, S. H., Javadi, A. H. et al. 2024. Improving the Performance of Smart Waterflooding Through Surfactant-Assisted Process for a Carbonate Oil Reservoir. Paper presented at the SPE Western Regional Meeting, Palo Alto, California, USA, 16−18 April. https://doi.org/10.2118/218844-MS.

Belhaj, A. F., Fakir, S. H., Singh, N. et al. 2023a. A Comparative Enhanced Oil Recovery Study Between Low-Salinity Water and Hybrid Surfactant Process for A Carbonate Reservoir. Paper presented at the SPE Western Regional Meeting, Anchorage, Alaska, USA, 22−25 May. https://doi.org/10.2118/212959-MS.

Belhaj, A. F., Fakir, S. H., Singh, N. et al. 2023b. Extensive Experimental Study of Low-Salinity Waterflooding Using Hele-Shaw Cell: A Focus on Gravity and Mobility Ratio Effects. Paper presented at the SPE Canadian Energy Technology Conference and Exhibition, Calgary, Alberta, Canada, 15−16 March. https://doi.org/10.2118/212785-MS.

Belhaj, A. F., Singh, N., and Sarma, H. K. 2022. Understanding the Interactions at Rock-Water and Oil-Water Interfaces during Controlled-Salinity Water Flooding. Paper presented at the Offshore Technology Conference Asia, Virtual and Kuala Lumpur, Malaysia, 22−25 March. https://doi.org/10.4043/31656-MS.

Berg, S., Ott, H., Klapp, S. A. et al. 2013. Real-Time 3D Imaging of Haines Jumps in Porous Media Flow. *Proc Natl Acad Sci U S A* **110** (10): 3755–3759. https://doi.org/10.1073/pnas.1221373110.

Borysenko, A., Clennell, B., Sedev, R. et al. 2009. Experimental Investigations of the Wettability of Clays and Shales. *J Geophys Res* **114** (B7). https://doi.org/10.1029/2008JB005928.

Buades, A., Coll, B., and Morel, J.-M. 2008. Nonlocal Image and Movie Denoising. *Int J Comput Vis* **76** (2): 123–139. https://doi.org/10.1007/s11263-007-0052-1.

Buckley, J. S., Liu, Y., and Monsterleet, S. 1998. Mechanisms of Wetting Alteration by Crude Oils. *SPE J.* **3** (01): 54–61. https://doi.org/10.2118/37230-PA.

Buckley, J. S., Liu, Y., Xie, X. et al. 1997. Asphaltenes and Crude Oil Wetting—The Effect of Oil Composition. *SPE J.* **2** (02): 107–119. https://doi.org/10.2118/35366-PA.

Cao, R., Sun, C., and Ma, Y. Z. 2015. Modeling Wettability Variation during Long-Term Water Flooding. *J Chem* **2015**: 1–11. https://doi.org/10.1155/2015/592951.

Caruana, A. and Dawe, R. A. 1996. Flow Behaviour in the Presence of Wettability Heterogeneities. *Transp Porous Med* **25** (2): 217–233. https://doi.org/10.1007/BF00135857.

Cha, L., Feng, Q., Wang, S. et al. 2023. Pore-Scale Modeling of Immiscible Displacement In Porous Media: The Effects of Dual Wettability. *SPE J.* **28** (01): 239–250. https://doi.org/10.2118/210589-PA.

Cnudde, V. and Boone, M. N. 2013. High-Resolution X-Ray Computed Tomography in Geosciences: A Review of the Current Technology and Applications. *Earth Sci Rev* **123**: 1–17. https://doi.org/10.1016/j.earscirev.2013.04.003.

Donaldson, E. C., Thomas, R. D., and Lorenz, P. B. 1969. Wettability Determination and Its Effect on Recovery Efficiency. *SPE J.* **9** (1): 13–20. https://doi.org/10.2118/2338-PA.

Drelich, J. W. 2019. Contact Angles: From Past Mistakes to New Developments through Liquid-Solid Adhesion Measurements. *Adv Colloid Interface Sci* **267**: 1–14. https://doi.org/10.1016/j.cis.2019.02.002.

Downloaded from http://onepetro.org/SJ/article-pdf/30/01/180/4110338/spe-223938-pa.pdf/1 by Tsinghua University user on 15 May 2025

Fakir, S. H., Belhaj, A. F., Singh, N. et al. 2023. Paper presented at the SPE Western Regional Meeting, Anchorage, Alaska, USA, 22−25 May. https://doi.org/10.2118/213020-MS.

Geistlinger, H. and Ataei-Dadavi, I. 2015. Influence of the Heterogeneous Wettability on Capillary Trapping in Glass-Beads Monolayers: Comparison between Experiments and the Invasion Percolation Theory. *J Colloid Interface Sci* **459**: 230–240. https://doi.org/10.1016/j.jcis.2015.07.074.

Gerami, A., Alzahid, Y., Mostaghimi, P. et al. 2018. Microfluidics for Porous Systems: Fabrication. *Microsc Appl Transp Por Med* **130** (1): 277–304. https://doi.org/10.1007/s11242-018-1202-3.

Herring, A. L., Gilby, F. J., Li, Z. et al. 2018. Observations of Nonwetting Phase Snap-off during Drainage. *Adv Water Resour* **121**: 32–43. https://doi.org/10.1016/j.advwatres.2018.07.016.

Herring, A. L., Sheppard, A., Andersson, L. et al. 2016. Impact of Wettability Alteration on 3D Nonwetting Phase Trapping and Transport. *Int J Greenh Gas Control* **46**: 175–186. https://doi.org/10.1016/j.ijggc.2015.12.026.

Holtzman, R. and Segre, E. 2015. Wettability Stabilizes Fluid Invasion into Porous Media via Nonlocal, Cooperative Pore Filling. *Phys Rev Lett* **115** (16). https://doi.org/10.1103/PhysRevLett.115.164501.

Ju, Y., Gong, W., and Zheng, J. 2019. Characterization of Immiscible Phase Displacement in Heterogeneous Pore Structures: Parallel Multicomponent Lattice Boltzmann Simulation and Experimental Validation Using Three-Dimensional Printing Technology. *Int J Multiphase Flow* **114**: 50–65. https://doi.org/10.1016/j.ijmultiphaseflow.2019.02.006.

Khishvand, M., Alizadeh, A. H., Oraki Kohshour, I. et al. 2017. In Situ Characterization of Wettability Alteration and Displacement Mechanisms Governing Recovery Enhancement Due to Low-salinity Waterflooding. *Water Resour Res* **53** (5): 4427–4443. https://doi.org/10.1002/2016WR020191.

Khishvand, M., Oraki Kohshour, I., Alizadeh, A. H. et al. 2019. A Multi-Scale Experimental Study of Crude Oil-Brine-Rock Interactions and Wettability Alteration during Low-Salinity Waterflooding. *Fuel (Lond)* **250**: 117–131. https://doi.org/10.1016/j.fuel.2019.02.019.

Klise, K. A., Moriarty, D., Yoon, H. et al. 2016. Automated Contact Angle Estimation for Three-Dimensional X-Ray Microtomography Data. *Adv Water Resour* **95**: 152–160. https://doi.org/10.1016/j.advwatres.2015.11.006.

Laben, A. B., Kayiem, H. H. A.-, Alameen, M. A. et al. 2022. Experimental Study on the Performance of Emulsions Produced during ASP Flooding. *J Petrol Explor Prod Technol* **12** (7): 1797–1809. https://doi.org/10.1007/s13202-021-01409-6.

Lei, W., Gong, W., and Wang, M. 2023. Wettability Effect on Displacement in Disordered Media under Preferential Flow Conditions. *J Fluid Mech* **975**. https://doi.org/10.1017/jfm.2023.879.

Lei, W., Lu, X., Liu, F. et al. 2022. Non-Monotonic Wettability Effects on Displacement in Heterogeneous Porous Media. *J Fluid Mech* **942**. https://doi.org/10.1017/jfm.2022.386.

Li, A., Li, R., Yan, C. et al. 2023. The Effect of Clay Type and Solid Wettability on Bitumen Extraction from Canadian Oil Sands. *Fuel (Lond)* **337**: 126887. https://doi.org/10.1016/j.fuel.2022.126887.

Liu, F. and Wang, M. 2020. Review of Low Salinity Waterflooding Mechanisms: Wettability Alteration and Its Impact on Oil Recovery. *Fuel (Lond)* **267**: 117112. https://doi.org/10.1016/j.fuel.2020.117112.

Liu, F. and Wang, M. 2022. Wettability Effects on Mobilization of Ganglia during Displacement. *Int J Mech Sci* **215**: 106933. https://doi.org/10.1016/j.ijmecsci.2021.106933.

Liu, G., Wang, H., Tang, J. et al. 2023. Effect of Wettability on Oil and Water Distribution and Production Performance in a Tight Sandstone Reservoir. *Fuel (Lond)* **341**: 127680. https://doi.org/10.1016/j.fuel.2023.127680.

Lusic, H. and Grinstaff, M. W. 2013. X-Ray-Computed Tomography Contrast Agents. *Chem Rev* **113** (3): 1641–1666. https://doi.org/10.1021/cr200358s.

Lv, P., Liu, Y., Wang, Z. et al. 2017. In Situ Local Contact Angle Measurement in a CO_2-Brine-Sand System Using Microfocused X-Ray CT. *Langmuir* **33** (14): 3358–3366. https://doi.org/10.1021/acs.langmuir.6b04533.

Mamonov, A., Kvandal, O. A., Strand, S. et al. 2019. Adsorption of Polar Organic Components onto Sandstone Rock Minerals and Its Effect on Wettability and Enhanced Oil Recovery Potential by Smart Water. *Eng Fuels* **33** (7): 5954–5960. https://doi.org/10.1021/acs.energyfuels.9b00101.

Menke, H., Bijeljic, B., Andrew, M. et al. 2014. Dynamic Pore-Scale Imaging of Reactive Transport in Heterogeneous Carbonates at Reservoir Conditions. *Energy Procedia* **63**: 5503–5511. https://doi.org/10.1016/j.egypro.2014.11.583.

Mohammed, M. and Babadagli, T. 2015. Wettability Alteration: A Comprehensive Review of Materials/Methods and Testing the Selected Ones on Heavy-Oil Containing Oil-Wet Systems. *Adv Colloid Interface Sci* **220**: 54–77. https://doi.org/10.1016/j.cis.2015.02.006.

Moura, M., Flekkøy, E. G., Måløy, K. J. et al. 2019. Connectivity Enhancement Due to Film Flow in Porous Media. *Phys Rev Fluids* **4** (9): 9. https://doi.org/10.1103/PhysRevFluids.4.094102.

Ott, H., Andrew, M., Snippe, J. et al. 2014. Microscale Solute Transport and Precipitation in Complex Rock during Drying. *Geophys Res Lett* **41** (23): 8369–8376. https://doi.org/10.1002/2014GL062266.

Quéré, D. 2008. Wetting and Roughness. *Annu Rev Mater Res* **38** (1): 71–99. https://doi.org/10.1146/annurev.matsci.38.060407.132434.

Reynolds, C. A., Blunt, M. J., and Krevor, S. 2018. Multiphase Flow Characteristics of Heterogeneous Rocks From CO_2 Storage Reservoirs in the United Kingdom. *Water Resour Res* **54** (2): 729–745. https://doi.org/10.1002/2017WR021651.

Saif, T., Lin, Q., Gao, Y. et al. 2019. 4D in Situ Synchrotron X-Ray Tomographic Microscopy and Laser-Based Heating Study of Oil Shale Pyrolysis. *Appl Energy* **235**: 1468–1475. https://doi.org/10.1016/j.apenergy.2018.11.044.

Sarma, H. K., Singh, N., Belhaj, A. F. et al. 2022. A Lab-to-Field Approach and Evaluation of Low-Salinity Waterflooding Process for High-Temperature High-Pressure Carbonate Reservoirs. Paper presented at the SPE Asia Pacific Oil & Gas Conference and Exhibition, Adelaide, Australia, 17−19 October. https://doi.org/10.2118/210657-MS.

Schlüter, S., Sheppard, A., Brown, K. et al. 2014. Image Processing of Multiphase Images Obtained via X-ray Microtomography: A Review. *Water Resour Res* **50** (4): 3615–3639. https://doi.org/10.1002/2014WR015256.

Schmatz, J., Urai, J. L., Berg, S. et al. 2015. Nanoscale Imaging of Pore-scale Fluid-fluid-solid Contacts in Sandstone. *Geophys Res Lett* **42** (7): 2189–2195. https://doi.org/10.1002/2015GL063354.

Selem, A. M., Agenet, N., Gao, Y. et al. 2021. Pore-Scale Imaging and Analysis of Low Salinity Waterflooding in a Heterogeneous Carbonate Rock at Reservoir Conditions. *Sci Rep* **11** (1). https://doi.org/10.1038/s41598-021-94103-w.

Shi, K.-Y., Chen, J.-Q., Pang, X.-Q. et al. 2023. Wettability of Different Clay Mineral Surfaces in Shale: Implications from Molecular Dynamics Simulations. *Pet Sci* **20** (2): 689–704. https://doi.org/10.1016/j.petsci.2023.02.001.

Shokri, N. and Or, D. 2013. Drying Patterns of Porous Media Containing Wettability Contrasts. *J Colloid Interface Sci* **391**: 135–141. https://doi.org/10.1016/j.jcis.2012.08.074.

Singh, K., Bijeljic, B., and Blunt, M. J. 2016. Imaging of Oil Layers, Curvature and Contact Angle in a Mixed-Wet and a Water-Wet Carbonate Rock. *Water Resour Res* **52** (3): 1716–1728. https://doi.org/10.1002/2015WR018072.

Singh, K., Bultreys, T., Raeini, A. Q. et al. 2022. New Type of Pore-Snap-off and Displacement Correlations in Imbibition. *J Colloid Interface Sci* **609**: 384–392. https://doi.org/10.1016/j.jcis.2021.11.109.

Downloaded from http://onepetro.org/SJ/article-pdf/30/01/180/4110338/spe-223938-pa.pdf/1 by Tsinghua University user on 15 May 2025

Singh, K., Menke, H., Andrew, M. et al. 2017. Dynamics of Snap-off and Pore-Filling Events during Two-Phase Fluid Flow in Permeable Media. *Sci Rep* **7** (1). https://doi.org/10.1038/s41598-017-05204-4.

Wang, H., Tian, L., Kang, K. et al. 2022. Characterization of Ultrasonic-Induced Wettability Alteration under Subsurface Conditions. *Langmuir* **38** (1): 514–522. https://doi.org/10.1021/acs.langmuir.1c02932.

Wildenschild, D. and Sheppard, A. P. 2013. X-Ray Imaging and Analysis Techniques for Quantifying Pore-Scale Structure and Processes in Subsurface Porous Medium Systems. *Adv Water Resour* **51**: 217–246. https://doi.org/10.1016/j.advwatres.2012.07.018.

Yang, J. and Zhou, Y. 2020. An Automatic In Situ Contact Angle Determination Based on Level Set Method. *Water Resour Res* **56** (7). https://doi.org/10.1029/2020WR027107.

Zhang, Y., Lin, Q., Raeini, A. Q. et al. 2022. Pore-Scale Imaging of Asphaltene Deposition with Permeability Reduction and Wettability Alteration. *Fuel (Lond)* **316**: 123202. https://doi.org/10.1016/j.fuel.2022.123202.

Downloaded from http://onepetro.org/SJ/article-pdf/30/01/180/4110338/spe-223938-pa.pdf/1 by Tsinghua University user on 15 May 2025